ORIGINAL ARTICLE

In situ S-isotope compositions of sulfate and sulfide from the 3.2 Ga Moodies Group, South Africa: A record of oxidative sulfur cycling

Sami Nabhan[1] 🆔 | Johanna Marin-Carbonne[2,3] 🆔 | Paul R.D. Mason[4] 🆔 | Christoph Heubeck[1]

[1]Department for Geosciences, Friedrich-Schiller-Universität Jena, Jena, Germany

[2]Laboratoire Magma et Volcans, Univ Lyon, UJM Saint Etienne, UBP, CNRS, IRD, St Etienne, France

[3]Institute of Earth Sciences, Universitè of Lausanne, Lausanne, Switzerland

[4]Department of Earth Sciences, Utrecht University, Utrecht, The Netherlands

Correspondence
Sami Nabhan, Friedrich-Schiller-Universität Jena, Institute for Geosciences, Burgweg 11, 07749 Jena, Germany
Email: nabhan@ipgp.fr

Present address
Sami Nabhan, Institute de Physique du Globe de Paris, Sorbonne Paris Cité, Université Paris Diderot, CNRS-UMR 7154, Paris, France

Funding information
Centre National de la Recherche Scientifique, Grant/Award Number: H2020 / 759289; Deutsche Forschungsgemeinschaft, Grant/ Award Number: He2418/13-1 and SPP 1833, Building a Habitable Earth; H2020 European Research Council, Grant/Award Number: 654208 / 17-EPN3-074 and 759289

Abstract

Sulfate minerals are rare in the Archean rock record and largely restricted to the occurrence of barite (BaSO$_4$). The origin of this barite remains controversially debated. The mass-independent fractionation of sulfur isotopes in these and other Archean sedimentary rocks suggests that photolysis of volcanic aerosols in an oxygen-poor atmosphere played an important role in their formation. Here, we report on the multiple sulfur isotopic composition of sedimentary anhydrite in the ca. 3.22 Ga Moodies Group of the Barberton Greenstone Belt, southern Africa. Anhydrite occurs, together with barite and pyrite, in regionally traceable beds that formed in fluvial settings. Variable abundances of barite versus anhydrite reflect changes in sulfate enrichment by evaporitic concentration across orders of magnitude in an arid, nearshore terrestrial environment, periodically replenished by influxes of seawater. The multiple S-isotope compositions of anhydrite and pyrite are consistent with microbial sulfate reduction. S-isotope signatures in barite suggest an additional oxidative sulfate source probably derived from continental weathering of sulfide possibly enhanced by microbial sulfur oxidation. Although depositional environments of Moodies sulfate minerals differ strongly from marine barite deposits, their sulfur isotopic composition is similar and most likely reflects a primary isotopic signature. The data indicate that a constant input of small portions of oxidized sulfur from the continents into the ocean may have contributed to the observed long-term increase in $\Delta^{33}S_{sulfate}$ values through the Paleoarchean.

KEYWORDS

(Microbial) pyrite oxidation, Archean anhydrite, Archean sulfur cycle, microbial sulfate reduction

1 | INTRODUCTION

The abundance of detrital pyrite and uraninite in the Archean sedimentary record has been interpreted to indicate very low atmospheric oxygen levels (Burron et al., 2018; England, Rasmussen, Krapez, & Groves, 2002; Guy et al., 2012; Hofmann, Bekker, Rouxel, Rumble, & Master, 2009; Koglin, Frimmel, Minter, & Brätz, 2010). Moreover, the mass-independent fractionation (MIF) of sulfur isotopes (expressed as $\Delta^{33}S = \delta^{33}S - 1000 \times [1 + \delta^{34}S/1000]^{0.515}$; Farquhar, Bao,

& Thiemens, 2000) in sulfide and sulfate has been interpreted to reflect photochemical reactions in a very-low-oxygen atmosphere (Farquhar et al., 2000; Farquhar, Savarino, Airieau, & Thiemens, 2001; Farquhar & Wing, 2003; Kasting, 2001; Mojzsis, Coath, Greenwood, McKeegan, & Harrison, 2003; Pavlov & Kasting, 2002). The conventional view is that photochemical reactions produce two isotopically different sulfur reservoirs: sulfate aerosols with negative $\Delta^{33}S$ and elemental sulfur with positive $\Delta^{33}S$ (Farquhar et al., 2000, 2001; Farquhar & Wing, 2003; Mojzsis et al., 2003). Prerequisites for the preservation of these isotopically distinct reservoirs are the absence of an ozone layer, which enables deep penetration of UV radiation into the atmosphere, and the prevention of oxidative mixing between the two reservoirs (Farquhar et al., 2000, 2001; Farquhar & Wing, 2003; Mojzsis et al., 2003), which implies an atmospheric oxygen level below 10^{-5} PAL (Mojzsis et al., 2003; Pavlov & Kasting, 2002). Low atmospheric oxygen levels result in the suppression or the absence of sulfide weathering and are thus an explanation for estimated low seawater sulfate concentration prior to the great oxidation event (<200 μM to < 2.5 μM; Canfield, Habicht, & Thamdrup, 2000; Crowe et al., 2014; Habicht, Gade, Thamdrup, Berg, & Canfield, 2002).

Because oceanic sulfate was low during the Archean, sulfate deposits are relatively uncommon. Examples of preserved Archean sulfate deposits are known from the Indian Dharwar Craton (Hoering, 1989; Muller et al., 2017), the southern African Barberton Greenstone Belt (BGB; Bao, Rumble, & Lowe, 2007; Heinrichs & Reimer, 1977; Muller, Philippot, Rollion-Bard, & Cartigny, 2016; Roerdink, Mason, Farquhar, & Reimer, 2012), and the western Australian Warrawoona Group of the Pilbara Block (Farquhar et al., 2000; Mojzsis et al., 2003; Roerdink et al., 2012; Shen, Farquhar, Masterson, Kaufman, & Buick, 2009; Ueno, Ono, Rumble, & Maruyama, 2008). These deposits contain sulfate exclusively as barite, which is formed by hydrothermal or diagenetic processes or by redeposition of older barite deposits as detrital material (Bao et al., 2007; Lowe, Drabon, & Byerly, 2019; Muller et al., 2016; Reimer, 1980, 1990; Roerdink et al., 2012; Roerdink, Mason, Whitehouse, & Brouwer, 2016; Shen et al., 2009; Ueno et al., 2008). A possible evaporative gypsum precursor for some of these beds has been debated but is generally discounted (Buick & Dunlop, 1990; Lowe et al., 2019; Reimer, 1980; Shen et al., 2009). The barite shows consistently negative $\Delta^{33}S$ values that increase over time, with average $\Delta^{33}S$ of approximately – 1.3‰ in ca. 3.5 Ga deposits and closer to −0.5‰ in ca. 3.26 Ga deposits (Bao et al., 2007; Muller et al., 2016; Roerdink et al., 2012, 2016; Shen et al., 2009; Ueno et al., 2008). $\Delta^{33}S$ values indicate that the sulfate involved in their formation was partly derived from photolysis and atmospheric deposition in the Archean ocean. Therefore, these barite deposits record the complex interplay of atmosphere, seawater, hydrothermal sources, and sediment chemistry at the time of their formation (Bao et al., 2007; Farquhar et al., 2007; Muller et al., 2016, 2017; Philippot, Zuilen, & Rollion-Bard, 2012; Roerdink et al., 2012, 2016; Shen et al., 2009; Ueno et al., 2008). $\Delta^{33}S$ values in diagenetic pyrite within the barite beds are similarly negative to those of the barite, which is consistent with the involvement of microbial sulfate reduction (MSR) in the Archean sulfur cycle and its propensity to preserve preexisting MIF signatures while executing mass-dependent sulfur isotope fractionation (MDF) (Bao et al., 2007; Farquhar et al., 2001; Hofmann et al., 2009; Muller et al., 2016; Roerdink et al., 2012; Shen et al., 2009; Ueno et al., 2008). Despite the occurrence of both pyrite and barite with negative $\Delta^{33}S$ signatures, the Archean rock record as a whole seems to show a surplus of positive values, resulting in an unbalanced archive (Farquhar et al., 2007; Philippot et al., 2012; Strauss et al., 2013). However, bulk analyses of sulfur from modern drainages of Archean crustal blocks (Superior and Kaapvaal Craton) indicate that Archean crust as a whole shows a balanced $\Delta^{33}S$ signature (Torres et al., 2018). Therefore, the apparent imbalance may reflect the low preservation potential of gypsum and anhydrite, resulting in only rare occurrences of these minerals and their pseudomorphs (Buick & Dunlop, 1990; Golding & Walter, 1979; Lowe & Worrell, 1999). Anhydrite is preserved in highly metamorphosed strata at 2.7 Ga (Golding & Walter, 1979; Sighinolfi, Kronberg, Gorgoni, & Fyfe, 1980) but, along with gypsum, does not become abundant in the rock record until after 2.4 Ga (Cameron, 1983; Cameron & Hattori, 1987; Huston & Logan, 2004).

Here, we present secondary ion mass spectrometry (SIMS) in situ sulfur (S) isotopic compositions ($\delta^{34}S$ and $\Delta^{33}S$) of anhydrite, barite, and pyrite from ca. 3.22 Ga-old potential paleosols of the Moodies Group of the BGB (Figure 1). These regionally traceable beds contain silicified nodules (Figure 2) with quartz pseudomorphs after gypsum and numerous anhydrite inclusions representing remnants of sedimentary gypsum (Heubeck et al., 2016; Nabhan, Luber, Scheffler, & Heubeck, 2016a). These occurrences represent, to date, the oldest preserved sedimentary anhydrite and the only Paleoarchean anhydrite yet analyzed for its multiple S-isotopic composition. Here, we investigate the mechanisms in an Archean terrestrial and dominantly anoxic environment that could have enriched sulfate to the levels necessary for anhydrite and gypsum precipitation. We also assess the potential role of microbiological metabolisms in processing sulfur through different redox states in these environments.

2 | GEOLOGICAL BACKGROUND

The Barberton Greenstone Belt (BGB) in northeastern South Africa and Eswatini is part of the Archean Kaapvaal Craton. Its stratigraphic fill, the up to 16-km-thick Barberton Supergroup, is subdivided from base to top into the 8- to 10-km-thick, 3.57–3.3 Ga-old Onverwacht Group; the 2- to 3-km-thick, 3.26–3.225 Ga-old Fig Tree Group; and the up to 3.7-km-thick, 3.225–3.214 Ga-old Moodies Group (Byerly, Lowe, & Heubeck, 2018; Lowe & Byerly, 2007; Lowe, Byerly, & Heubeck, 1999; Figure 1a). Moodies Group rocks occupy large synclines throughout the greenstone belt (Figure 1a) and are mainly composed of polymict conglomerate, quartz-rich sandstone, and argillaceous siltstone deposited in terrestrial to shallow-marine environments (Heubeck, 2019; Heubeck & Lowe, 1999). Braided fluvial and braid-plain facies occur at several stratigraphic levels of the Moodies Group and can be tens to hundreds of meters thick (Figure 1b). Braided fluvial facies are stacked in wide and shallow channels with
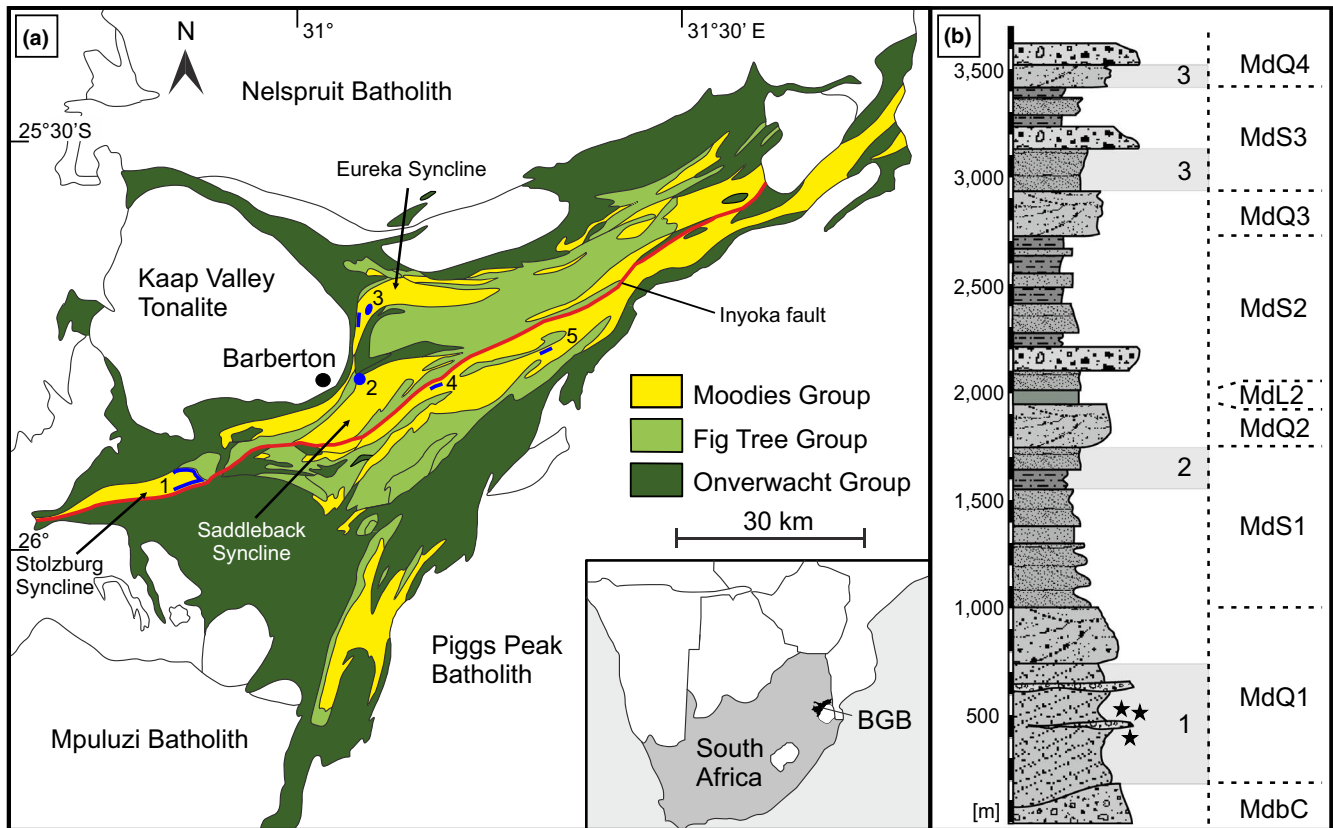
FIGURE 1 Geology of the Barberton Greenstone Belt (BGB) and the Moodies Group. (a) Generalized geological map of the BGB. Localities in blue mark sites with silicified gypsum nodules. (b) Generalized stratigraphy of the Moodies Group. Gray bars show stratigraphic positions of the localities in a. Locations 4 and 5 (not shown in column) could not be stratigraphically assigned because Moodies Group stratigraphy south of the Inyoka Fault is poorly known. Stratigraphic terminology follows Anhaeusser (1976). Black asterisks mark the approximate stratigraphic positions of the investigated beds (Fig. S1)

erosive bases composed of pebble strings, fining upward into cross-bedded granular to medium-grained sandstone overlain by rippled fine-grained sandstone and in places topped by mm-thin argillaceous siltstone showing desiccation cracks (Heubeck, 2019; Heubeck et al., 2016; Nabhan, Luber, et al., 2016). Braided fluvial strata are best preserved in the lower Moodies Group (MdQ1) of the Stolzburg Syncline (Figure S1). They contain regionally traceable beds with abundant, silicified gypsum nodules (Nabhan, Luber, et al., 2016; Figures 2 and 3). To date, nodules have been recorded at four stratigraphic levels in five locations throughout the BGB (Figure 1).

Nodules appear in up to 50-cm-thick beds and increase in number, size, and structural complexity toward the top of these beds (Figure 3). The beds are organized into 5- to 20-cm-thick upper horizons that largely lack relict sedimentary structures and are mainly composed of coalesced, broadly stratiform nodules (Figure 2b) within a matrix that contains high proportions of shale and reworked volcanic ash. Underlying sandier, up to 40-cm-thick horizons contain nodules that follow primary sedimentary structures such as horizontal stratification or foresets. Cross-cutting relations between overlying and adjacent channels show that nodules formed prior to lithification in presumably moist sediment. Superimposed channels that cut into nodule-bearing beds erode and subsequently redeposit nodules as clasts in coarse-grained

channel bases. Nodular textures and inclusion mineralogy vary laterally and vertically among nodule-bearing beds that have previously been interpreted as potential paleosols (Nabhan, Luber, et al., 2016). Commonly, nodules are composed of mega-quartz pseudomorphs after gypsum, calcite, and potentially barite. Abundant inclusions of anhydrite, barite, and calcite are 5–50 µm in size and appear only within the pseudomorphs (Figure 4). The inclusions and pseudomorphs are in places aligned along or resemble radial crystal fans (Figure 4). The observed mineralogical composition of inclusions presumably reflects the original sulfate and carbonate mineralogy for the nodules. However, the anhydrite inclusions possibly result from a gypsum precursor, and the high strontium content of some calcite inclusions implies an aragonite precursor (Nabhan, Luber, et al., 2016). Nodule-bearing beds also contain, in places, mm-scale heavy mineral laminations mainly composed of rounded detrital pyrite overgrown by euhedral early diagenetic pyrite (Nabhan, Wiedenbeck, Milke, & Heubeck, 2016b; Figure S2). Most beds with heavy mineral laminations have been affected by modern weathering with oxidation of pyrite, although many pyrite grains still show zoning seen elsewhere in unaltered pyrite grains (Figure 5c). Bending of lamination around nodules and the inclusion of pyrite with overgrowth rims indicate contemporaneous formation of nodules and pyrite overgrowths (Figures 2c and 5).
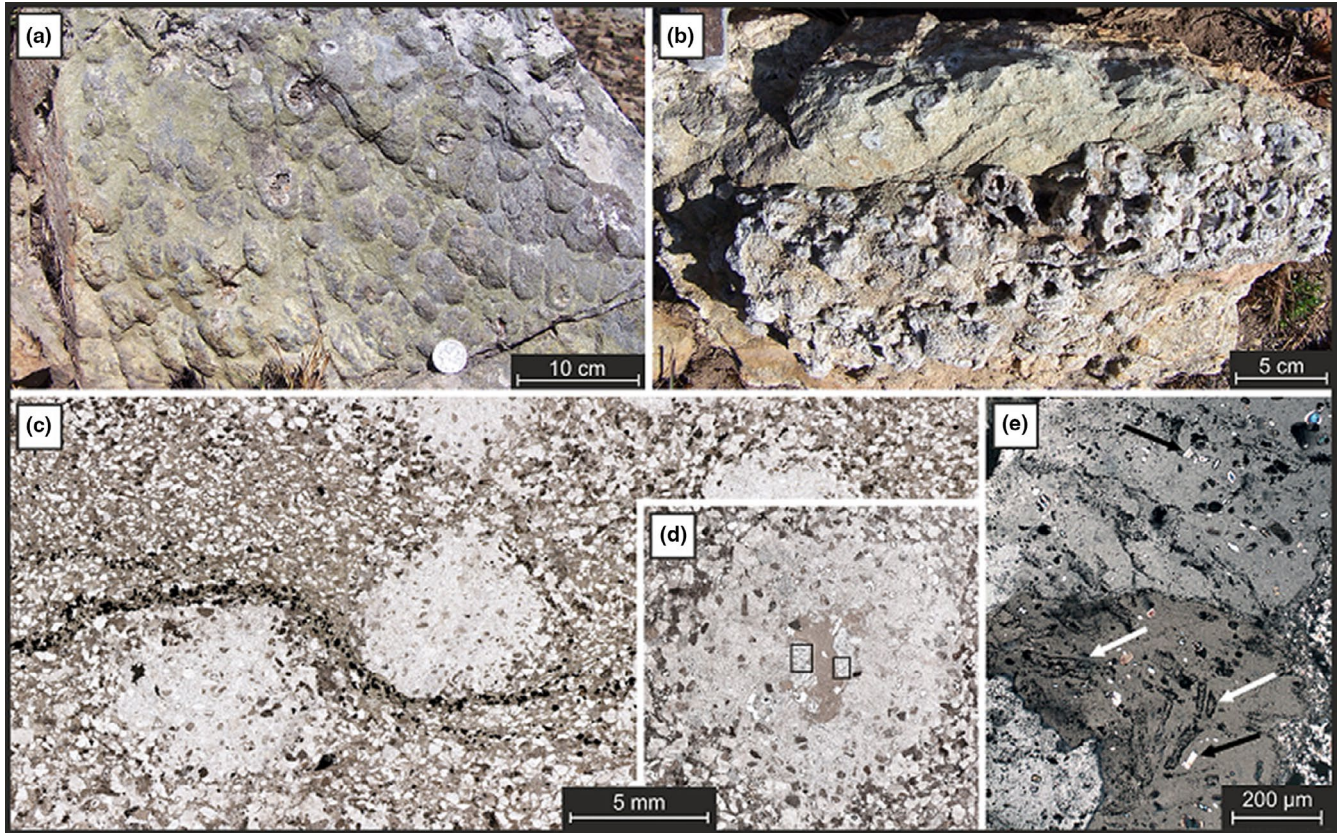
FIGURE 2 Sedimentary structures and textures of Moodies Group nodule-bearing beds and nodules. (a) Top view of bedding plane of a sandstone bed rich in silicified nodules. (b) Cross-sectional view of a sandstone bed with silicified, partly hollow rock-forming nodules. (c) Thin-section image of sample 12-003-4 showing several silicified nodules in medium-grained sandstone. The opaque grains defining a lamina are mainly composed of pyrite with accessory zircon, chromite, and apatite. (d) Thin-section image of a silicified nodule with a mica-filled central cavity and inward-pointing crystals. Black rectangle to the left is shown enlarged in e. (e) Polarized-light image of an inward-pointing quartz crystal with bright and colorful anhydrite inclusions (black arrows) and silicified crystal "ghosts" with dark edges (white arrows)

3 | SAMPLES

The in situ S-isotopic composition of anhydrite, barite, and pyrite was measured from three representative samples (12-003-4, 13-004-3 and 13-004-4) of the lower Moodies Group from the eastern Stolzburg Syncline (Figure 1; Figure S1). Sampled materials occur over > 100 m stratigraphic thickness and ca. 1 km horizontal distance. Nodules in these beds differ texturally and vary in size (3 mm to 3.5 cm). Nabhan, Luber, et al. (2016) distinguished four types of nodules and showed that their spatial distribution depended on their stratigraphic position above channel base: The smallest nodules with the simplest textural composition occur at a stratigraphically low position within a bed, while stratigraphically higher positioned nodules are larger and texturally more complex. Additionally, texturally simple nodules near the channel base contain mainly anhydrite inclusions while nodules in a stratigraphically higher position within the same bed contain more barite and fewer anhydrite inclusions. Complex and coalesced nodules at the top of nodule-bearing beds form cm-thick bedding-parallel horizons and contain numerous calcite and barite inclusions but lack anhydrite inclusions. Because of the highly energetic floodplain setting with mainly erosional channel bases, most nodule-bearing beds are not fully preserved. The beds sampled for this study are from three different

incomplete channels and could therefore not be assigned to specific heights above channel base. However, they show distinct textural and mineralogical features (Figures 4 and 6). Microscopic evaluation of thin sections and mounts shows quartz pseudomorphs after both gypsum and carbonate that correspond to variations in the inclusion mineralogy (Figures 4 and 6). Raman spectroscopy was used to characterize numerous mineral inclusions on and below the thin-section surface, including a number of fluid and gas inclusions within quartz that are commonly aligned along the edges of pseudomorphs. Sample 12-003-4 is from a ca. 30-cm-thick bed of medium-grained litharenite. It contains up to 1-cm-diameter nodules and mm-thick heavy-mineral laminae mainly composed of 50- to 300-μm-sized pyrite grains (Figure 2c). The nodules are composed of poikilotopic quartz and commonly contain a central zone composed of muscovite (Figures 2d and 6a). Inward-growing crystals in the nodules' core contain quartz pseudomorphs after gypsum with numerous anhydrite inclusions, while barite inclusions are rare (Figures 2e, 4c and d, and 6b). Sample 13-004-4 is from a ca. 40-cm-thick medium- to coarse-grained cross-bedded litharenite with large nodules up to 2 cm in diameter. The edges of the nodules are composed of poikilotopic quartz with inward-pointing crystals that contain numerous small pseudomorphs (Figures 4e, f, and 6c) with anhydrite and barite inclusions (Figure 6d). The core of these nodules is commonly
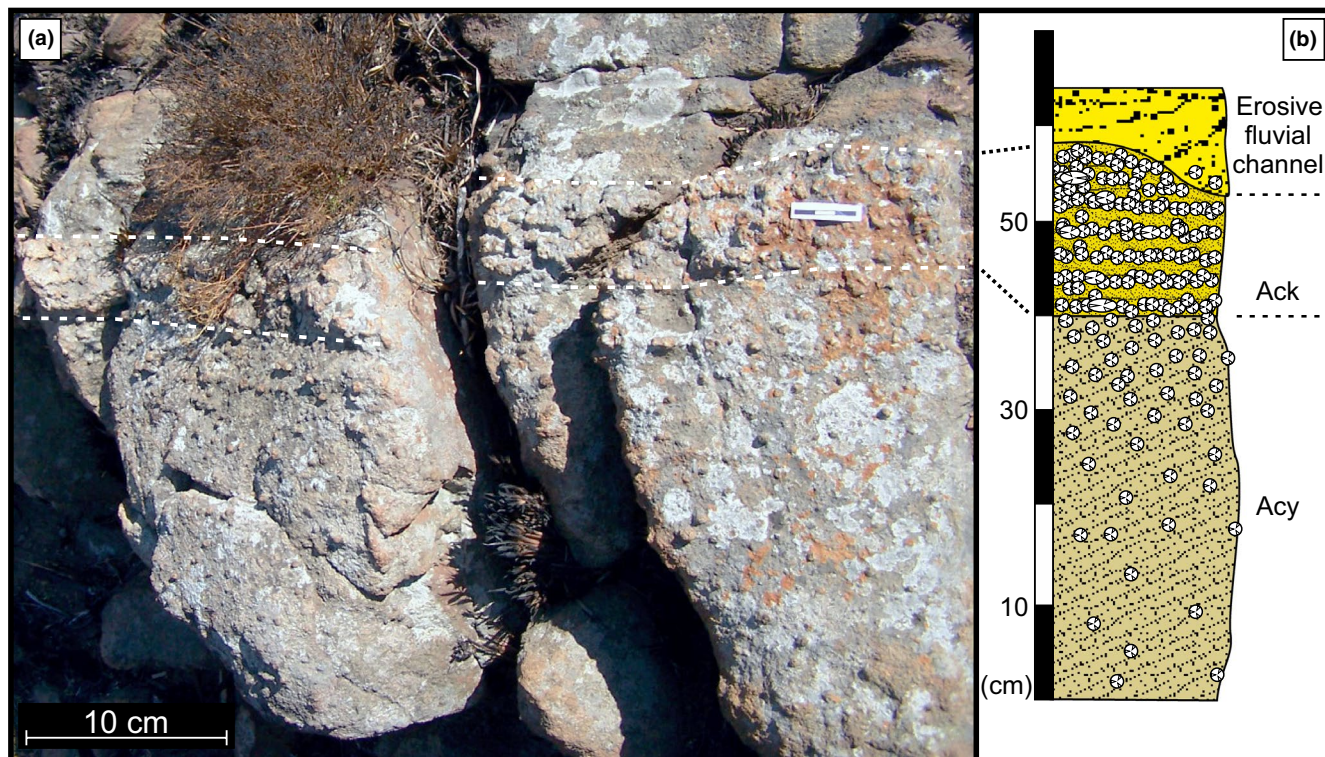
FIGURE 3 Internal subdevision of nodule-bearing beds. (a) Cross-sectional outcrop photograph of a ca. 30-cm-thick, nodule-bearing bed of medium- to coarse-grained sandstone with individual nodules at the base and a topping ca. 5 cm thick unit of coalesced nodules (dashed white lines), containing little detrital material. The nodule-bearing bed is overlain by nodule-free, low-angle cross-bedded, medium- to coarse-grained sandstone (b) Line drawing of typical nodule-bearing bed, showing possible Acy and Ack soil horizon subdivisions. Fluvial channels commonly erode deeply into these beds, reworking nodules as clasts

filled by inclusion-free clear quartz (Figure 6c). Pseudomorphs are typically anhedral and cannot clearly be assigned to a primary mineralogy (Figure 6d). The number of anhydrite and barite inclusions preserved in the nodules of this sample is approximately equal. Sample 13–004–3 is from a ca. 35-cm-thick bed of cross-bedded to planar-laminated medium-grained litharenite. The nodules are aligned along cross-bedding and lamination and reach up to 3 cm in size. They show a ca. 3- to 5-mm-thick outer edge of poikilotopic quartz followed by an up to 1-cm-thick zone of inward-pointing inclusion-rich quartz crystals and up to 5-mm-large muscovite-filled central zones (Figure 6e). All sulfate inclusions in sample 13-004-3 are composed of barite (Figure 6f), while numerous calcite inclusions are present within acicular, well-preserved quartz pseudomorphs (Figure 4a, b). From all mounts and thin sections characterized by optical microscopy and Raman spectroscopy, two thin sections or mounts from sample 12-003-4 were selected for S-isotopic analysis of pyrite and one from each sample was selected for S-isotopic analysis of sulfate inclusions.

4 | METHODS

4.1 | SIMS analysis

Sulfur isotope ratios were measured on the Cameca IMS 1280 HR2 (CRPG-CNRS, Nancy, France) during two analytical sessions by

simultaneous measurements of $^{32}S^-$, $^{33}S^-$, and $^{34}S^-$ in multicollection mode with three off-axis Faraday cups. The sulfur isotopic ratios of pyrite, anhydrite, and barite of sample 12-003-4 were measured during the first session, and the sulfur isotopic ratios of barite of sample 13-004-3 and sample 13-004-4 were measured during a second session. The analytical method is described in more detail in Thomassot et al. (2009) and Marin-Carbonne et al. (2014). A Cs^+ primary beam of 5 nA intensity was focused to a spot of about 15–20 μm to measure sulfides. Due to the lower S-emissivity of sulfate, a Cs^+ primary beam of 8 nA was used for measuring sulfate. Typical $^{32}S^-$ intensity was between 6 and $10*10^8$ counts per second (cps) for sulfide and between 4 and $6*10^8$ cps for sulfate. Several pyrite (Maine: $\delta^{34}S = -20.61‰$, $\delta^{33}S = -10.63‰$; Spain: $\delta^{34}S = -1.56‰$, $\delta^{33}S = -0.78‰$; and Balmat: $\delta^{34}S = +15.84‰$, $\delta^{33}S = +8.12‰$; Table S1a; Figure S3) and sulfate standards (Cuney: $\delta^{34}S = +13.8‰$; Taxco: $\delta^{34}S = +15.3‰$; $BaSO_4$: $\delta^{34}S = +22.8‰$; and Maiza: $\delta^{34}S = +27.7‰$, $\delta^{33}S = +14.2‰$; Table S1b; Figures S4 and S5) were used to determine (i) the instrumental mass fractionation and (ii) the reference mass discrimination line, from which $\Delta^{33}S$ values were calculated. Sulfur isotope compositions are expressed using delta notation ($\delta^{33}S$ and $\delta^{34}S$) relative to the international standard V-CDT based on the following equation:

$$\delta^2 S = \left[\left(^2S / ^1S_{sample} \right) / \left(^2S / ^1S_{standard} \right) - 1 \right] \times 1000.$$

FIGURE 4 Photomicrographs of silicified crystal fans from nodules. (a) Silicified crystal fan (sample 13-004-3) with acicular crystal outlines and aligned inclusions of calcite and barite. (b) Cathodoluminescence (CL) image of the same area. Quartz appears purple while a calcite inclusion within a crystal outline appears in bright orange, suggesting that the crystal fan was initially composed of carbonate. (c and d) Plane-light and polarized-light images, respectively, of a former crystal fan without "ghost" crystals (sample 12-003-4; black rectangle to the right in Figure 2d). The abundance of radially aligned anhydrite inclusions in the quartz crystal suggests its original composition as a Ca-sulfate crystal fan. (e) Translucent-light image of replacive mega-quartz crystals from sample 13-004-4 with few very small inclusions lacking ghost crystal outlines. (f) CL image of the same area. The replacive nature of the quartz crystals is apparent by numerous crystal outlines. The original mineralogy of the replaced crystals remains uncertain due to the lack of inclusions
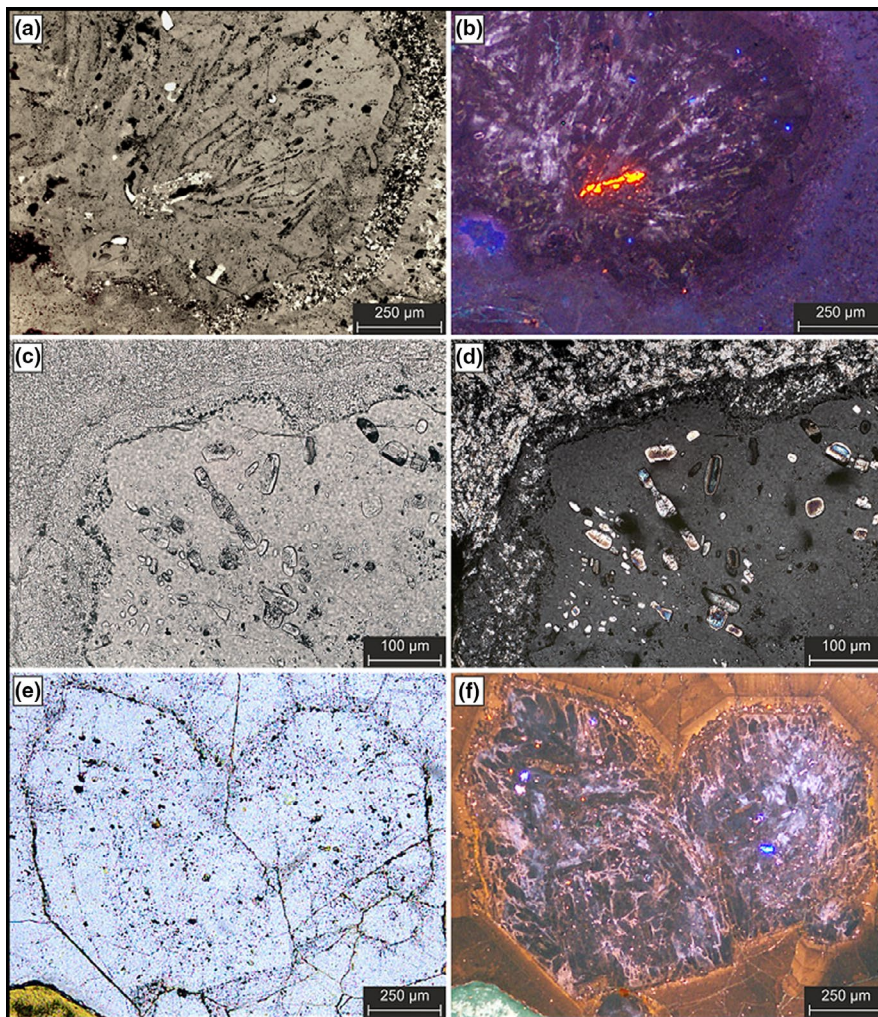
where 1 and 2 represent the heavy and light isotopes, respectively (34 or 33 and 32 for S). Mass-independent fractionation has been calculated as the deviation from the Terrestrial Fractionation Line (TFL), using the mass discrimination law (Farquhar et al., 2000):

$$\Delta^{33}S = \left(\ln\left(\frac{\delta^{33}S}{1000} + 1 \right) - 0.515 \times \ln\left(\frac{\delta^{34}S}{1000} \right) + 1 \right),$$

where the factor 0.515 defines the slope of the TFL.

A typical analysis consisted of 2 min of pre-sputtering in raster mode followed by data acquisition in 40 cycles of 5 s each. The background of the detectors was measured during pre-sputtering and was then corrected for each analysis. The internal precision achieved under these conditions was better than 0.05‰ for $\delta^{34}S$ and better than 0.03‰ for $\delta^{33}S$ values (2σ). The reproducibility was better than ± 0.40‰ (2σ) for $\delta^{34}S$ and ± 0.1‰ (2σ) for $\Delta^{33}S$ values for both sulfates and sulfide. The analytical uncertainty for pyrite was better than 0.23‰ for $\delta^{34}S$ values and 0.15‰ for $\delta^{33}S$ values. Analytical uncertainties for anhydrite were 0.17‰ for $\delta^{34}S$ values and 0.19‰ for $\delta^{33}S$ values. The analytical uncertainties for barite measured during the first session were 1.22‰ for $\delta^{34}S$ values and 0.64‰ for $\delta^{33}S$ values. For barite measured during the second

session, the analytical uncertainties were 0.60‰ for $\delta^{34}S$ values and 0.38‰ for $\delta^{33}S$ values. The high analytical uncertainty of the barite measured during the first session resulted from isotopic inhomogeneity of the barite standard $BaSO_4$ and was compensated by adding Maiza as barite standard in the second session. Errors of the mean values in the results section are given as standard deviations (1σ) of the described populations.

4.2 | Raman spectroscopy

Pyrite zoning was determined using reflected-light microscopy (Figure S2). Some pyrite grains contain up to 50 μm large inclusions of carbonaceous material (CM) that are either concentrated in the detrital cores or along the core–rim boundary (Figure 7). We used a Horiba LabRAM HR Evolution Confocal Raman Instrument with a focal length of 800 mm (Department of Geosciences, Friedrich-Schiller-University Jena) to characterize 20 inclusions of carbonaceous material within three pyrite grains to subsequently evaluate the thermal overprint of the analyzed samples by metamorphic or hydrothermal alteration. All Raman spectra were calibrated using an internal calibration objective with an imbedded polymer. For all
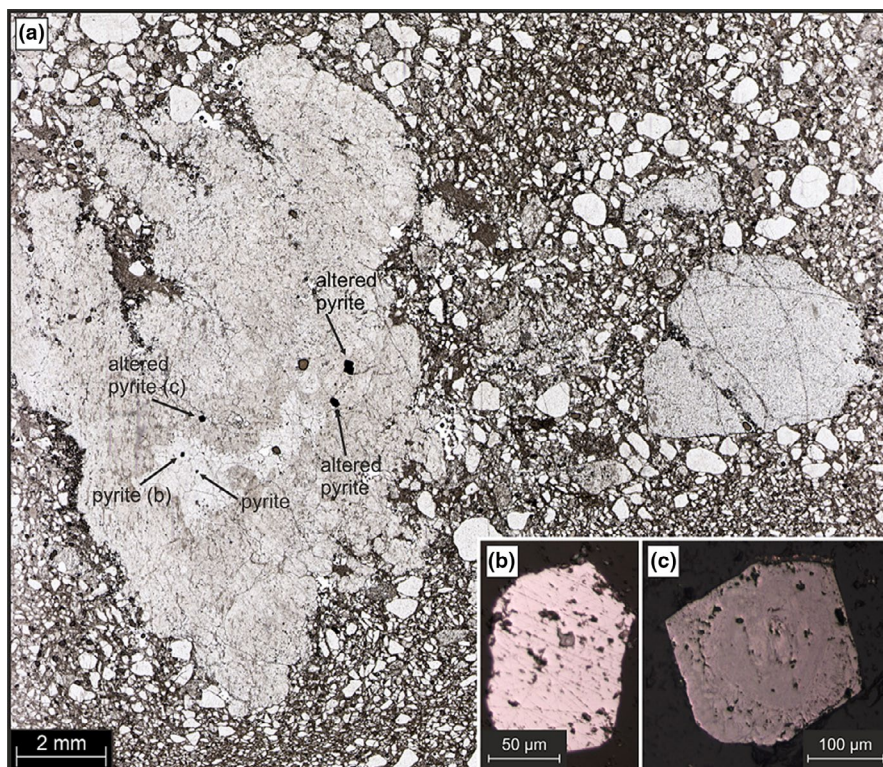
FIGURE 5 Microscopic images of redeposited nodule with inclusions of detrital pyrite and pyrite overgrowths (Sample 11–164 from Dycedale Syncline; location 2 in Figure 1). (a) Plane-light photomicrograph of a nodule (left) with irregular margins in a coarse-grained to granular sandstone adjacent to a chert granule (right). The nodule contains several pyrite and altered pyrite grains (black arrows). (b) Reflected-light image of a pyrite grain in the nodule showing typical shape of idiomorphic overgrowth. (c) Reflected-light image of a former pyrite crystal altered by modern weathering and now composed of hematite and goethite. Despite its oxidation, the grain still shows a rounded core outline and euhedral overgrowth as the unaltered pyrite grains in Figure 7 and in Figure S2

measurements, a 532 nm laser was used combined with a 600 gr/mm grating and a 100x-VIS objective. We used an exposure time of 30 to 60 s with two accumulations. Laser power was reduced to ca. 250 µW to avoid oxidation of any adjacent pyrite and destruction of the CM. CM spectra were evaluated to calculate a maximum metamorphic temperature. The position, intensity, and area of the G, D1, and D2 peaks were extracted using the peak-characterization tool of LabSpec 6 by fitting them with Voigt functions (Figure 7c). Temperatures were calculated using the area ratio of D1/(G + D1 + D2) = R2. The calculated temperatures are based on the geothermometers of Beyssac, Goffe, Chopin, and Rouzaud (2002) and Aoya et al. (2010) for regional and contact-metamorphic rocks (Table S2). These thermometers can be used for a temperature range of approximately 300 to 650°C. Both have an estimated error of ± 50°C. Calculated R1 values for CM range between 1.62 and 1.92, while R2 values range from 0.65 to 0.70. Temperatures calculated from these values vary between 331°C and 352°C with an average of 340°C (Table S2).

5 | SULFUR ISOTOPIC COMPOSITIONS

5.1 | S-isotopes of anhydrite and barite

S-isotopes (^{32}S, ^{33}S, and ^{34}S) were measured in 46 sulfate inclusions from the three samples. Of the inclusions, 11 were anhydrite (sample 12-003-4) and 35 barite (all samples). The $\delta^{34}S$ composition of the anhydrite ranges from +10.45‰ to +2.82‰ with a mean of

+5.33‰ ± 2.34‰ (Table 1; Figure 8). Anhydrite $\Delta^{33}S$ values range from −0.14‰ to −0.50‰ with a mean of −0.28‰ ± 0.13‰. The $\delta^{34}S$ composition of barite ranges from +9.79‰ to −0.43‰ with a mean of +3.11‰ ± 1.97‰. Barite $\Delta^{33}S$ values range from +0.19‰ to −0.39‰ with a mean of −0.18‰ ± 0.13‰. Barite inclusions show corresponding variations between the three samples. Barite inclusions from sample 12-003-4 (n = 4) show the heaviest $\delta^{34}S$ values from +9.79‰ to +3.24‰ with a mean of +6.65‰ ± 2.80‰. The respective $\Delta^{33}S$ values range from −0.05‰ to −0.34‰ with a mean of −0.23‰ ± 0.13‰. $\delta^{34}S$ values of barite from sample 13-004-4 (n = 13) range from +4.73‰ to +2.21‰ with a mean of +3.65‰ ± 0.64‰. $\Delta^{33}S$ values range from +0.09‰ to −0.39‰ with a mean of −0.24‰ ± 0.09‰. $\delta^{34}S$ values of barite from sample 13-004-3 (n = 18) range from +3.70‰ to −0.43‰ with a mean of +1.93‰ ± 1.19‰. The respective $\Delta^{33}S$ values range from +0.19‰ to −0.35‰ with a mean of +0.12‰ ± 0.14‰ (Figure 8; Table 1; Table S1c). While the $\delta^{34}S$ composition of the sulfates is highly variable, most $\Delta^{33}S$ values are close to −0.25‰ and overlap partly, but are mainly more positive than those of previously investigated Paleoarchean barite deposits (Figure 8b).

5.2 | S-isotopes of pyrite

S-isotopes were measured in 24 pyrite grains from two mounts of sample 12-003-4, including detrital cores and secondary overgrowths. Samples that include material from both zones in their analysis volume are referred to as transitional pyrite (Table S1d).
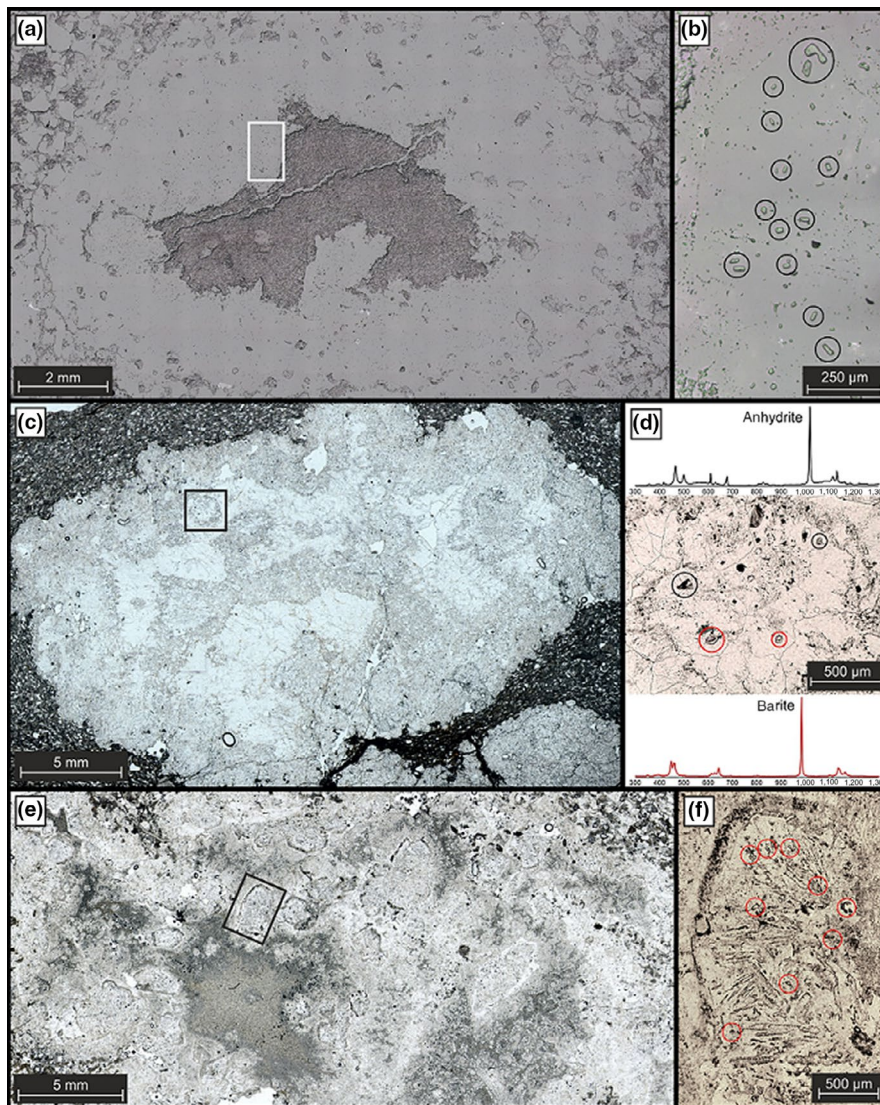
FIGURE 6 Microphotographs of nodules with sulfate inclusions. (a) Silicified nodule (sample 12-003-4) showing muscovite-filled central cavity. An inward-facing crystal marked by the white rectangle is shown in b. (b) Inward-growing quartz crystal with numerous inclusions. Circled inclusions were identified by Raman spectroscopy as anhydrite, and those large enough were analyzed for their multiple sulfur isotopic composition (Table S1c). (c) Thin-section image of a silicified nodule (sample 13-004-4) composed of inclusion-rich quartz (outer areas) and inclusion-free quartz (inner, bright areas). The area in the black rectangle is shown in d. (d) Numerous small former sulfate crystals, largely but not completely replaced by quartz, within a larger quartz crystal. The original mineralogy of the larger crystal outlined by dark anhedral margins is unknown, but numerous barite (red circles; Raman spectrogram below) and anhydrite (blue circles; Raman spectrogram above) inclusions are present in approximately equal proportions. (e) Thin-section image of a silicified nodule (sample 13-004-3); medium-gray area shows the central nodule cavity, filled by muscovite. Note numerous inward-facing quartz pseudomorphs. Area outlined by black rectangle is shown in f. (f) Replacive quartz crystal incorporating numerous silicified, radial acicular crystals. Dark outlines are defined by numerous very small (μm-sized) sulfate and carbonate inclusions. Barite inclusions are marked by red circles

$\delta^{34}S$ values of detrital cores (n = 35) range from +4.91‰ to −1.96‰ with a mean of +1.07‰ ± 1.89‰. $\Delta^{33}S$ values vary between +0.38‰ and −0.25‰ with a mean of +0.03‰ ± 0.11‰. Overgrowths (n = 16) show $\delta^{34}S$ values from −10.62‰ to −24.05‰ with a mean of −19.68 ± 3.76‰. Corresponding $\Delta^{33}S$ values range from −0.10‰ to −0.33‰ with a mean of −0.25 ± 0.06‰. $\delta^{34}S$ values of the transitional pyrite (n = 24) range from +0.74‰ to −14.84‰ with a mean of −7.65‰ ± 5.19‰. The respective $\Delta^{33}S$ values range from +0.21‰ to −0.31‰ with a mean of −0.10‰ ± 0.12‰ (Figure 8; Table 1; Table S1d).

5.3 | Comparison of isotopic values

The $\delta^{34}S$ values of detrital pyrite cores and secondary pyrite overgrowths largely overlap with the values presented by Nabhan, Wiedenbeck, et al. (2016). A correlation between the S-isotopic composition and the texture (e.g., porous or non-porous) to the provenance of the detrital pyrite as previously suggested (England et al., 2002; Nabhan, Wiedenbeck, et al., 2016) could not be found. A frequency distribution diagram (Figure 9) of all $\delta^{34}S$ values shows that the largest group (about 32%) of detrital pyrite shows values
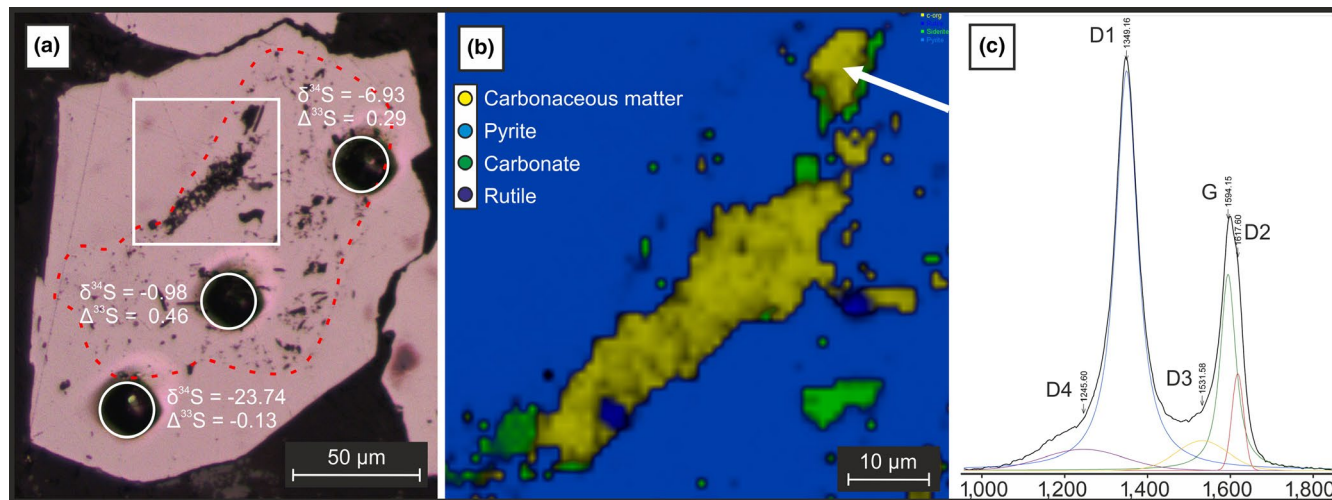
FIGURE 7 Pyrite morphology, S-isotopes, and inclusion composition. (a) Reflected-light image of pyrite grain A (Table S2) showing a porous detrital core (marked by dashed line) and a homogenous secondary rim. Results of S-isotope analyses are shown next to the SIMS pits (white circles). The white rectangle marks the area shown in b. (b) Raman map of opaque inclusions in pyrite, mainly composed of carbonaceous material but also of carbonate and rutile. White arrow marks the position of the Raman spectrum shown in c. (c) Raman spectrum of carbonaceous material. The area ratio (R2; Beyssac et al., 2002) of the peaks indicates a maximum temperature of ca. 340°C (Table S2). X-axis is Raman-shift in cm^{-1}

TABLE 1 Range of S-isotopic composition of S-minerals in analyzed beds; *n* = number of analyses

Sample	Mineral	*n*	$\delta^{34}S$ (‰)			$\Delta^{33}S$ (‰)		
			Min	Max	Mean	Min	Max	Mean
12-003-4	Anhydrite	11	+2.82	+10.45	+5.33 ± 2.34	−0.50	−0.14	−0.28 ± 0.13
	Barite	4	+3.24	+9.79	+6.65 ± 2.80	−0.34	−0.05	−0.23 ± 0.13
	Detrital pyrite	35	−1.96	+4.91	+1.07 ± 1.89	−0.25	+0.38	−0.03 ± 0.11
	Transitional pyrite	24	−14.84	+0.74	−7.65 ± 5.19	−0.31	+0.21	−0.10 ± 0.12
	Pyrite overgrowth	16	−24.05	−10.62	−19.68 ± 3.76	−0.33	−0.10	−0.25 ± 0.06
13-004-4	Barite	13	+2.21	+4.73	+3.65 ± 0.64	−0.39	−0.09	−0.24 ± 0.09
13-004-3	Barite	18	−0.43	+3.70	+1.93 ± 1.19	−0.35	+0.19	−0.12 ± 0.14

around 3‰. A similar distribution can be seen in the $\delta^{34}S$ values of the barite from sample 13-004-3 that have a similarly high maximum (ca. 39%) at 3‰ and almost as many values around 2‰ (ca. 22%). The distribution of $\delta^{34}S$ values of anhydrite and barite from sample 12-003-4 is slightly shifted toward heavier values with the largest number of analyses at 4‰ and heavier (Figure 9a), but the relatively low number of analyses (*n* = 15) might have biased the distribution. The overlap of the maxima of detrital pyrite and barite of sample 13-004-3 might imply a connection between these two groups; however, the frequency distribution (Figure 9b) of their $\Delta^{33}S$ values shows only a minor overlap. A strong overlap in the $\Delta^{33}S$ values is observed between the sulfate inclusions and the pyrite overgrowths of sample 12-003-4. Both have the largest number of $\Delta^{33}S$ values in the range between −0.15‰ and −0.3‰. The similarity of the $\Delta^{33}S$ values of sulfate inclusions and pyrite overgrowths, in combination with the large difference in their $\delta^{34}S$ values, suggests that their isotopic values may result from the mass-dependent fractionation of a single sulfur source that resulted in a $\delta^{34}S_{sulfate}-\delta^{34}S_{sulfide}$ fractionation of up to 34‰.

6 | DISCUSSION

The sulfate and carbonate nodules of the Moodies Group occur in strata of braided-fluvial to supratidal depositional setting throughout the BGB. The nodules have previously been interpreted as syn-sedimentary to early diagenetic in origin, based mainly on the stratification of nodule-bearing beds, cross-cutting relations with adjacent fluvial channels, and the reworking and redeposition of nodules in fluvial channels superimposed on nodule-bearing beds (Heubeck, 2019; Heubeck et al., 2016; Nabhan, Luber, et al., 2016). The origin of the sulfate required to form these nodules remains unclear, especially considering the generally low estimates for sulfate concentrations in Archean oceans and surface waters (< 200 µM; Canfield et al., 2000; Crowe et al., 2014; Habicht et al., 2002). High levels of seawater sulfate as a consequence of oxidative sulfur cycling are responsible for the relative abundance of sulfate minerals in modern environments. However, the Archean atmosphere was low in oxygen as evidenced by the MIF-S record and the widespread transport
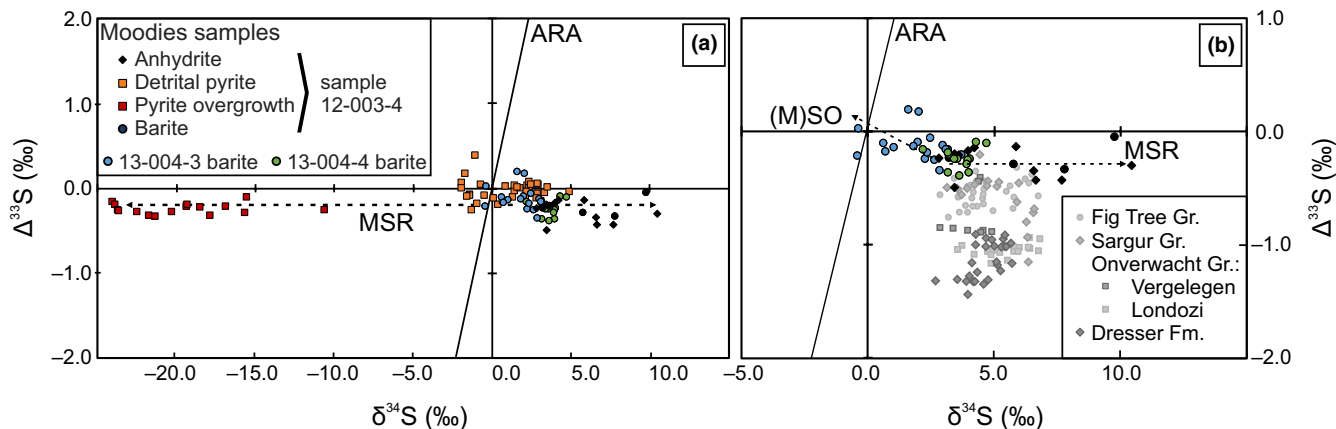
FIGURE 8 Sulfur isotopic composition ($\delta^{34}S$ versus $\Delta^{33}S$) of anhydrite, barite, and pyrite from Moodies Group nodule-bearing beds. (a) Analyzed anhydrite and pyrite are from sample 12–003–4. Pyrite overgrowths and anhydrite show similar mean $\Delta^{33}S$ values of −0.25‰ and −0.28‰ but an up to 34‰ fractionation in their $\delta^{34}S$ composition, indicating MDF by MSR (dashed arrows). The S-isotopic composition of the detrital pyrite reflects a juvenile source but also contribution by some MIF sulfur. Variations in the S-isotopic composition of anhydrite and barite are shown in detail in b. ARA: Archean reference array. (b) $\delta^{34}S$ versus $\Delta^{33}S$ composition of Paleoarchean sulfates. Moodies sulfates show higher $\Delta^{33}S$ values and larger $\delta^{34}S$ variations than other documented Paleoarchean barite deposits (for details, see Bao et al., 2007; Farquhar et al., 2001; Hoering, 1989; Muller et al., 2017; Roerdink et al., 2012; Shen et al., 2009; Ueno et al., 2008). The heavy $\delta^{34}S$ values of barite and anhydrite in sample 12-003-4 are possibly due to MSR. The light $\delta^{34}S$ and partly positive $\Delta^{33}S$ values from barite of sample 13-004-4 possibly resulted from pyrite oxidation. The homogeneous S-isotopic composition of the barite of sample 13-004-4 is interpreted as representing the mixing of ocean water sulfate with sulfate from pyrite oxidation

and deposition of detrital pyrite and uraninite (Burron et al., 2018; England et al., 2002; Guy et al., 2012; Hofmann et al., 2009; Koglin et al., 2010). This would have significantly inhibited or eliminated oxidative sulfide weathering as a sulfate source. In the following discussion, we explore how the necessary sulfate enrichment for anhydrite and gypsum nodule formation could have been possible, and whether or not this was facilitated by biological processes.

6.1 | Nodule formation

The formation of stratified nodule beds predating compaction and the high proportion of unstable detrital feldspar and lithic grains preserved within the nodules characterize these beds as primitive Aridisols (Mack, James, & Monger, 1993; Nabhan, Luber, et al., 2016; Retallack, 1993) with calcareous upper and gypsiferous lower horizons (Figure 3). The formation of gypsum or anhydrite nodules in an Archean surface environment requires sulfate levels to be locally and temporarily two to four orders of magnitude higher than typically estimated for the Archean ocean that vary between < 200 µM and 2.5 µM (Figure 10; Canfield et al., 2000; Crowe et al., 2014; Habicht et al., 2002). This necessitates a sulfate enrichment process such as evaporative brine formation or oxidative sulfide weathering. However, the presence of preserved detrital and early diagenetic pyrite in the same rocks is a strong argument against extensive oxidative weathering in this depositional environment. The Moodies floodplains were characterized by recurring phases of desiccation, indicated by the abundance of mud-cracked shales (Heubeck, 2019; Heubeck et al., 2016; Nabhan, Luber, et al., 2016). Desiccation could have increased sulfate concentrations in brines sufficiently

to precipitate gypsum. Overlying coastal, tidal, and deltaic strata (Heubeck, 2019; Heubeck et al., 2016) show the proximity of the floodplains to the ocean. In this environment, sea spray and frequent groundwater incursions of Archean seawater with subsequent repetitive evaporative periods in semi-arid braid plains could have been plausible sulfate accumulation mechanisms. Drying–wetting periods in the vadose zone caused by variable precipitation, combined with reduced or interrupted sediment supply, would have provided favorable conditions for a fluctuating groundwater table. This, in turn, could have created favorable conditions for pedogenic and early diagenetic growth of evaporative nodules during dry periods associated with rising groundwater (Retallack, 1991). The formation of nodules in such a system could have resulted in the different nodule types that correlate with vertical height above channel-fill base (Chandler, 1988; Chowns & Elkins, 1974; Retallack, 1991). Due to the lack of typical pedogenic weathering products such as clay minerals and the largely evaporative nature of the nodules, we argue that nodule-bearing horizons are closely related to sabkha-type surfaces. Nevertheless, their formation at, or close to, the surface places these beds at the intersection of the lithosphere and the atmosphere with the involvement of the hydrosphere via groundwater fluctuations and evaporation.

6.1.1 | Silicification

Most nodules show two distinctly different zones of quartz (Figures 4e and f; Figure 5a; Figure 6c,e; and Figure 11a). All nodules have an outer zone of poikilotopic mega-quartz and inward-pointing crystals with numerous pseudomorphs, in part forming radial crystal fans.
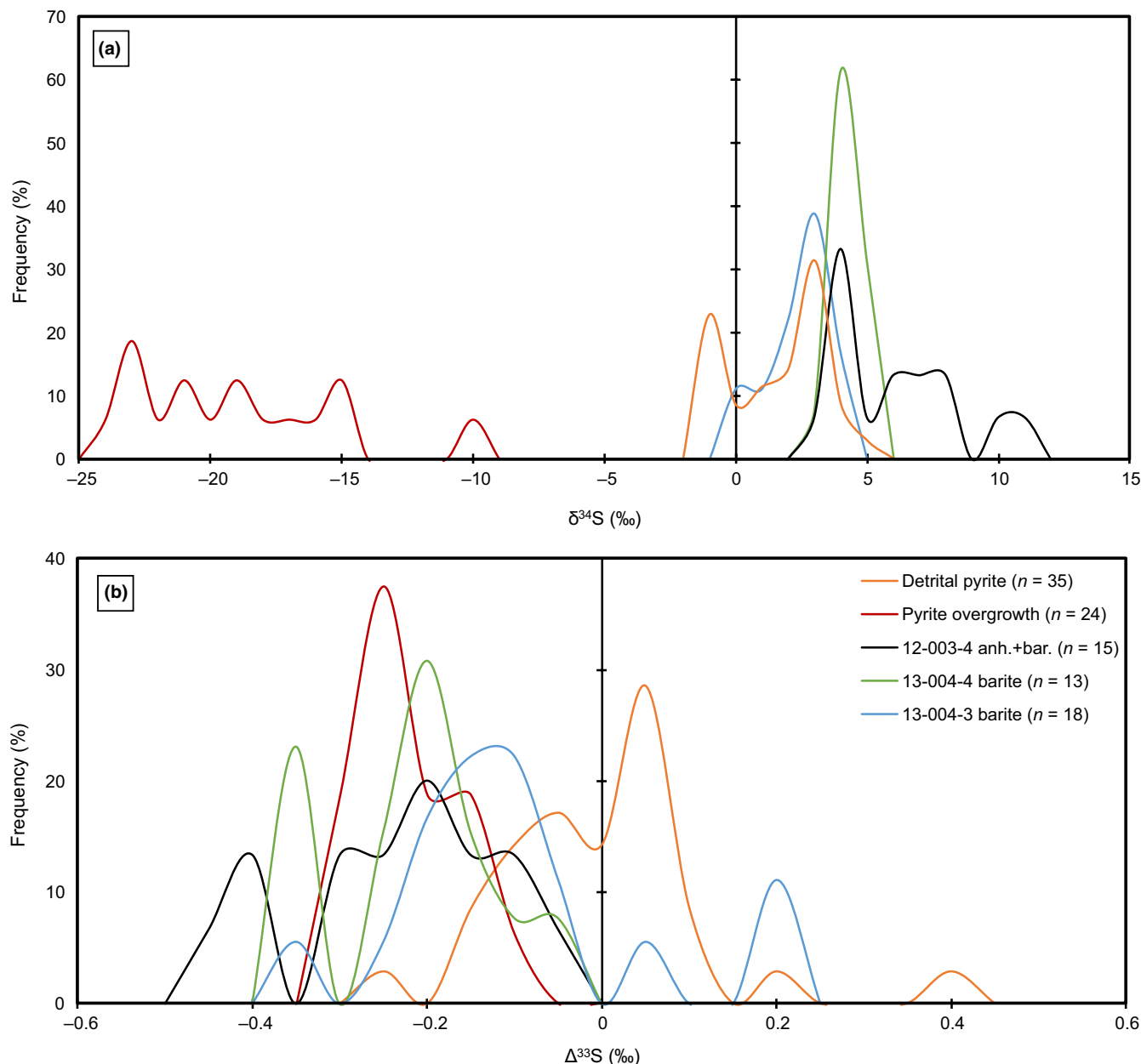
FIGURE 9 Frequency distribution of S-isotopes of Moodies sulfates and pyrite. (a) Frequency distribution diagram of $\delta^{34}S$ values calculated in 1‰ steps. (b) Frequency distribution diagram of $\Delta^{33}S$ values calculated in 0.05‰ steps. The legend in b applies to both graphs

Sulfate and carbonate inclusions are almost exclusively restricted to this zone and to the pseudomorphs therein. This zone represents the part of the nodules that was initially composed of evaporitic minerals (sulfates and carbonates); its formation was interpreted as early-diagenetic replacive silicification of evaporitic minerals (Heubeck, 2019; Heubeck et al., 2016; Nabhan, Luber, et al., 2016). Such an early-diagenetic silicification is a prerequisite for stabilizing the nodules and preventing them from possible dissolution, especially in the case of their redeposition. However, some nodules interpreted as redeposited show irregular shapes, indicating partial dissolution (Figure 5a). This implies that redeposition of nodules was possible even before silicification. Nonetheless, silicification must have taken place prior to compaction because the nodules show no sign

of compaction-related deformation. The preservation of delicate textures such as radial crystal fans (Figure 4a-d) in which interstitial spaces between crystals still visible as color change in CL (white versus purple in Figure 4b) is a strong argument for early-diagenetic silicification of the outer zone. Fluid inclusions aligned along the edges of pseudomorphs are composed of water, in places with a central gas bubble of H_2S (Figure 11). The H_2S gas in these inclusions may represent the product of sulfate reduction that took place during the silicification of the nodules.

The inner quartz zone is a result of a later phase of silicification and is free of sulfate or carbonate inclusions. This quartz commonly overgrows the pseudomorphous inward-growing crystals of the first silicification event (Figures 4e,f, 6e) and fills former central cavities
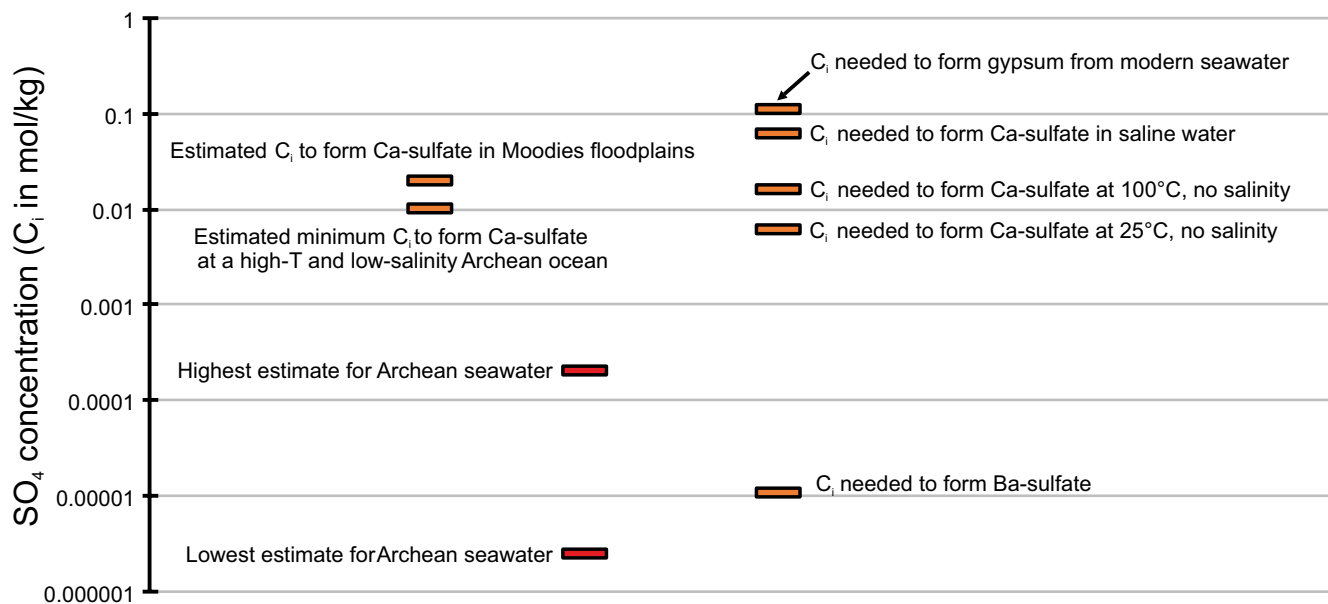
FIGURE 10 Estimated sulfate concentrations. Estimates of sulfate concentration in Archean seawater vary between 2.5 and 200 µM (Canfield et al., 2000; Crowe et al., 2014; Habicht et al., 2002). Sulfate saturation values to form Ca- and Ba-sulfates are well-known from thermodynamic modeling and experiments. They may vary according to temperature, salinity, or pressure (Babel & Schreiber, 2014; Bock, 1961; Partridge & White, 1929). Sulfate concentrations leading to the precipitation of Ca-sulfate in the supratidal environment of Moodies floodplains are approximations because salinity and temperature of the Archean ocean are poorly constrained

within the nodules (Figures 5a and 6c). The quartz of this zone is commonly intergrown with muscovite (Figures 4c,d, 6e, and 11a) which is also widespread as fill of central cavities (Figs. 2d, 6a,). The intergrowth of the quartz with muscovite and their common appearance are similar to the metamorphic quartz-sericite fabric of the Moodies sandstone throughout the BGB (Heubeck, 2019; Heubeck & Lowe, 1999). We argue therefore that this second phase of silicification took place during greenschist-facies or hydrothermal alteration of the BGB.

6.1.2 | Potential metasomatic alteration

Syn-depositional and early post-depositional hydrothermal and metasomatic alteration of Moodies Group strata is known from the Saddleback Syncline and other areas adjacent to the Lomati River Sill in the center of the BGB (Heubeck, 2019). There, Moodies sandstone is intensely silicified within a ca. 1-km-thick halo around the sill and is cross-cut in places by shallow subvolcanic dikes (Heubeck, 2019). Unit MdQ1 in the Stolzburg Syncline shows no cross-cutting dikes, and the fabric of the nodules that are composed of megaquartz is distinctly different from the microcrystalline texture resulting from hydrothermal silicification. A juvenile sulfate source due to syn-depositional hydrothermal activity is unlikely throughout unit MdQ1 of the Stolzburg Syncline because of the lack of any accompanying mappable structures. Hydrothermally introduced sulfate would presumably result in the formation of barite specifically along fluid pathways due to the extremely low solubility of barite (Davis & Collins, 1971; Babel & Schreiber, 2014), which is inconsistent

with the strict limitation of barite to the nodules. A bedding-parallel formation of carbonate or anhydrite nodules that contain barite (Figures 2 and 3) is more readily explained by interactions between a diagenetic sulfate-bearing pore fluid and a diagenetic Ba-containing pore fluid in unconsolidated sediment. The barium in these fluids was likely provided by the decomposition of detrital Ba-feldspars (Nabhan, Luber, et al., 2016). Furthermore, the common occurrence of former carbonate-dominated nodules would require such a hydrothermal fluid to be variably enriched in both sulfate and carbonate. These substantial variations are more readily explained by evaporation-driven formation from a seawater source. However, it remains possible that hydrothermal fluids were mixed with seawater sulfate prior to the accumulation of this sulfate in Moodies sediments, as proposed for Fig Tree barite (Bao et al., 2007; Muller et al., 2016; Roerdink et al., 2012).

6.2 | Pyrite origin and formation

6.2.1 | Detrital pyrite

The S-isotopic composition of pyrite in Moodies nodule-bearing beds is highly variable (Figures 7–9; Table S1d) and reflects the two populations of detrital cores and overgrowths. Detrital pyrite is difficult to relate to sulfur processing within the nodule-bearing beds because its age and origin mirror the provenance of the sedimentary rocks. The scatter of the values with $\delta^{34}S = -1.96$ to $+4.91‰$ and $\Delta^{33}S$ values close to $\pm 0‰$ largely overlaps with those of pyrites from the underlying Fig Tree and the Onverwacht Groups (Farquhar
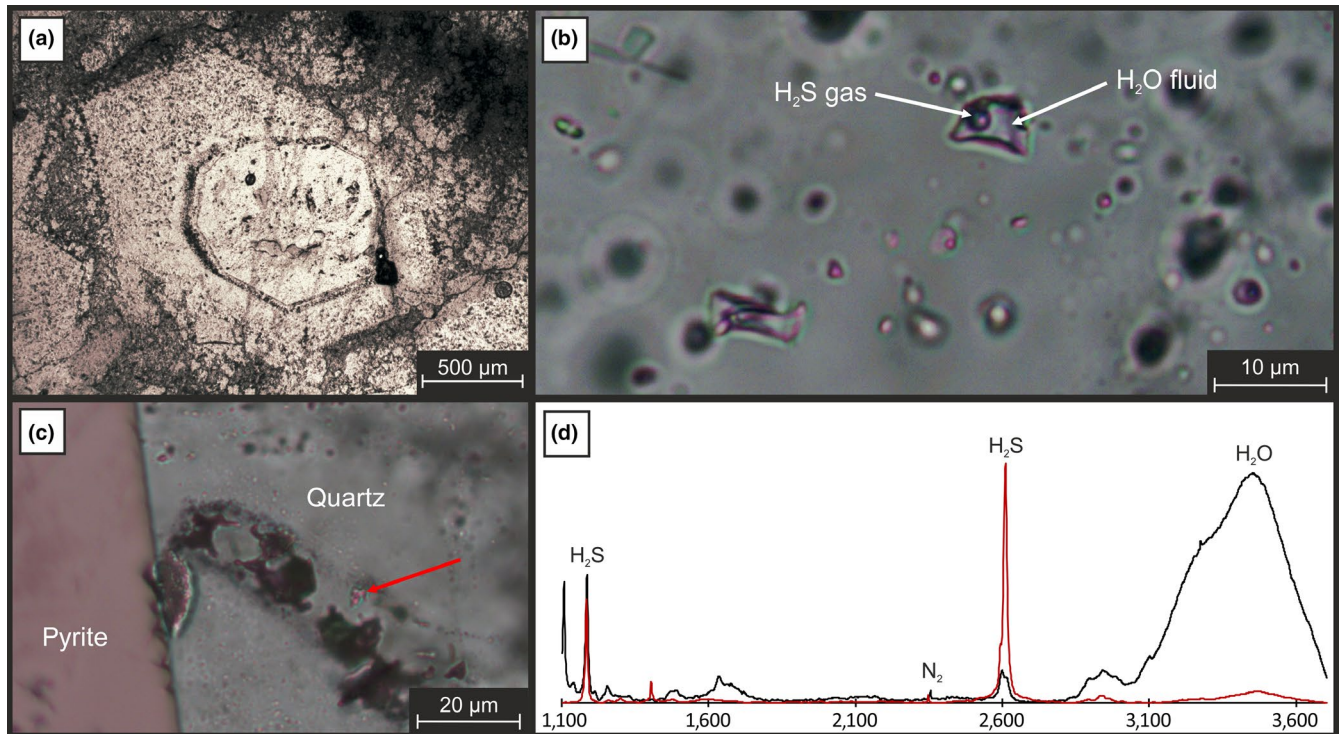
FIGURE 11 Fluid and gas inclusions in silicified nodules. (a) Inward-facing inclusion-rich quartz pseudomorph overgrown by a second quartz phase, intergrown with sericitic muscovite. The second overgrowth is free of sulfate or carbonate inclusions (sample 13-004-3). (b) Fluid and gas inclusions from the silicified quartz pseudomorph in a. The inclusions contain water as fluid and a gas bubble composed of H_2S. (c) Contact zone of a silicified nodule (sample 12–003–4) with an euhedral pyrite overgrowth. The fluid and gas inclusions of this sample commonly show a strong H_2S-Raman signal (see d). (d) Raman spectra of the two inclusions shown in b and c with X-axis as Raman-shift in cm^{-1}. The spectrum of the inclusion in b (plotted in black) shows a very strong water signal and a weak but clear H_2S signal. The spectrum of the inclusion in c (plotted in red) shows a weak water and a strong H_2S signal. Both spectra show also an extremely weak N_2 signal, likely an atmospheric contribution during the measurement

et al., 2007; Grosch & McLaughlin, 2013; Ohmoto, Kakegawa, & Lowe, 1993; Philippot et al., 2012; Roerdink et al., 2016; Roerdink, Mason, Whitehouse, & Reimer, 2013) and largely resembles previously measured values of massive detrital pyrite in the same strata. However, a correlation between the S-isotopic composition and the texture or provenance of the detrital pyrite, as previously suggested (England et al., 2002; Nabhan, Wiedenbeck, et al., 2016), could not be reproduced.

6.2.2 | Pyrite overgrowth

Pyrite overgrowths are typically euhedral and fully enclose detrital cores (Figure 6a; Figure S2). Their incorporation into gypsum nodules (Figure 5) indicates their penecontemporaneous formation with sulfate mineral precipitation. Late hydrothermal sulfide mineralization is common in the northern part of the BGB (e.g., the Eureka Syncline; Figure 1a). It affected the Moodies Group at approximately 3.1 to 3.0 Ga and led to the formation of paragenetic arseno- and chalcopyrite, with a distinct absence of sulfate (Agangi, Hofmann, Eickmann, Marin-Carbonne, & Reddy, 2016; Agangi, Hofmann, & Przybyłowicz, 2014; Otto, Dziggel, Kisters, & Meyer, 2007). In contrast, the analyzed samples are free of paragenetic sulfides and contain only

pyrite. Furthermore, the overgrowths are mostly free of arsenic, the most common trace element of the late hydrothermal pyrite (Agangi et al., 2016), and show substantially higher nickel concentrations, while cobalt concentrations are commonly low, resulting in Co/Ni ratios of the overgrowths < 0.4 (Nabhan, Wiedenbeck, et al., 2016). These ratios are substantially lower than ratios reported from hydrothermal pyrite in the northern BGB (Agangi et al., 2014) and consistent with an authigenic or diagenetic origin (Gregory et al., 2015), while hydrothermal pyrite commonly shows Co/Ni ratios around 2 or higher (Large et al., 2009). Raman spectroscopic analyses of inclusions of carbonaceous material within pyrites from the nodule-bearing beds yields a metamorphic temperature of 340°C ± 50°C (Figure 6 and Table S3). Postulated maximum temperatures for the hydrothermal event reach up to 680 ± 25°C (Otto et al., 2007), but the majority of the hydrothermal sulfides in the northern BGB formed at temperatures around 300°C (de Ronde, Spooner, Wit, & Bray, 1992) and show mainly positive $\delta^{34}S$ values (Agangi et al., 2016). It is thus highly unlikely that the negative $\delta^{34}S$ values of the pyrite overgrowth resulted from thermochemical sulfate reduction (TSR) during the hydrothermal mineralization in the BGB. At approximately 300°C, the $\delta^{34}S$ fractionation between the resulting sulfide and the sulfate source would be below 20‰ (Rye, 2005). The observed $\delta^{34}S$ fractionation between anhydrite and pyrite overgrowths

of up to 34‰ requires a low-temperature regime (< 150°C), close to the minimum temperature for TSR of ca. 130°C (Machel, 2001; Worden, Smalley, & Oxtoby, 1995) if the pyrite formed from the observed anhydrite (Rye, 2005). A formation of the anhydrite and the pyrite by TSR from a common sulfate source would still require temperatures below 180°C (Rye et al., 2005). We therefore argue that the pyrite overgrowths are not related to this pulse of mineralization but are early-diagenetic and substantially older.

6.3 | Implications for sulfate concentration

The formation of barite requires sulfate levels to be at least 10 µM (Davis & Collins, 1971; Babel & Schreiber, 2014). The formation of Ca-sulfate (gypsum or anhydrite) would require SO_4 concentrations to be several orders of magnitude higher since the lowest possible saturation of sulfate in solution to form these minerals at 25°C and 1 bar is approximately 16 mM (Figure 10; Bock, 1961; Babel & Schreiber, 2014). With increasing temperature, the saturation of sulfate to form both minerals drops toward ca. 6 mM at 100°C. Gypsum remains the dominant and stable phase below 40°C, while anhydrite starts to form at higher temperatures and becomes the dominant phase at temperatures around 90°C (Figure 10; Partridge & White, 1929; Babel & Schreiber, 2014). The solubility of anhydrite and gypsum at 25°C and 1 bar in freshwater is 2.75 g/L and 2.07 g/L, respectively. An increasing concentration of other phases in solution such as NaCl can increase the solubility of calcium sulfate up to ca. 8.3 g/L but cannot lead to a reduction (Bock, 1961). In turn, the concentration of sulfate in solution to reach saturation with respect to calcium sulfate increases with increasing salinity to about 60 mM. In modern environments, the concentration of SO_4 needs to be approximately 110 mM to form gypsum from seawater (Babel & Schreiber, 2014). This concentration appears to be implausible to reach from Archean seawater before reaching the saturation point to form halite. However, the overall salinity of the Archean ocean remains poorly constrained with estimates ranging from slightly lower than modern seawater (Marty, Avice, Beakaert, & Broadley, 2018) to twice as high as modern seawater (Knauth, 2005). Estimates for the salinity of Archean seawater based on fluid inclusions in quartz are strongly dependent on assumed paleotemperature of the Archean ocean, with higher temperatures resulting in a lower salinity (Marty et al., 2018). Archean seawater of presumably low salinity and high temperature could therefore reach saturation to precipitate Ca-sulfate already at a sulfate concentration of ca. 20 mM (Figures 10 and 12). High daytime temperatures in sabkhas are known from modern examples and would help to push the sulfate concentration needed to form Ca-sulfate minerals down to ca. 10 mM. They may even allow for an overall temperate climate.

The varying proportion of anhydrite to barite among the three analyzed beds indicate that the sulfate levels experienced fluctuations, implying high (>20 mM) sulfate levels where anhydrite is the dominant phase (sample 12-003-4; Figure 4c, d and 6a, b), possibly moderate sulfate (around 10–20 mM) where anhydrite and barite

are both present (13-004-4; Figures 6c, d, and 12), and low sulfate («10 mM) where anhydrite is absent (13-004-3; Figures 6e, f, and 12). The dominance of calcite inclusions in nodules that lack anhydrite implies that brines were here not enriched enough in sulfate to form anhydrite or gypsum. The precipitation of Ca-carbonate, however, shows that a low Ca^{2+} concentration is unlikely to be the reason for the observed changes in mineralogy. A high concentration of Ba^{2+} could potentially reduce sulfate accumulation; this is, however, unlikely since Ba^{2+} availability by silicate weathering alone is limited compared to that of Ca^{2+}. The presence of both ions with sulfate levels of ca. 20 mM would still lead to the co-precipitation of Ba- and Ca-sulfate.

6.3.1 | Potential sulfate sources

It appears clear that seawater is the most likely sulfate source in a supratidal floodplain. Archean seawater sulfate was mainly derived from rainout of atmospheric sulfate aerosols that incorporated a negative $\Delta^{33}S$ signal, as demonstrated by Archean marine barite (Bao et al., 2007; Muller et al., 2016, 2017; Roerdink et al., 2012; Shen et al., 2009; Ueno et al., 2008). Its $\delta^{34}S$ composition has been estimated to be ca. −2‰, and values have been suggested to have been shifted by microbial processing such as MSR and mixing with juvenile hydrothermal sulfate in restricted basins to reach the $\delta^{34}S$ values of the Paleoarchean barite between +3‰ and +6‰ (Bao et al., 2007; Muller et al., 2016; Ohmoto et al., 1993; Roerdink et al., 2012; Shen et al., 2009; Ueno et al., 2008). However, the Moodies sulfate and sulfide multiple S-isotope data plot over a larger area than the field estimated for Archean seawater, extending toward more juvenile isotopic values (Figure 8b). Anhydrite inclusions from the Moodies nodules show a similar S-isotopic "fingerprint" that overlaps with that of the marine barite deposits from the Fig Tree Group (Fig. 8b and 12; Bao et al., 2007; Muller et al., 2016; Roerdink et al., 2012; Shen et al., 2009), while the barite inclusions of sample 13-004-3 are more variable and show the lowest $\delta^{34}S$ and highest $\Delta^{33}S$ values (Table 1, Figure 8 and Table S1c). The shift in the S-isotopic composition of the Moodies barite suggests the contribution of a second, possibly minor sulfate source that appeared when the supply of seawater sulfate was limited.

Potential sources are (1) juvenile sulfate from hydrothermal activity, (2) $\Delta^{33}S$-positive sulfate introduced by microbial sulfur disproportionation (MSD), or (3) sulfate produced by continental oxidative pyrite weathering, with an average S-isotopic composition similar or equivalent to juvenile sulfur. As argued before, it is highly unlikely that a syn-depositional hydrothermal source was contributing to the formation of the Moodies sulfates. MSD is equally unlikely because it should have processed predominantly $\Delta^{33}S$-positive S_0 aerosols (Farquhar & Wing, 2003; Grosch & McLaughlin, 2013; Philippot et al., 2007). Mixing of seawater sulfate with estimates for MSD-derived sulfate would produce higher $\delta^{34}S$ values than those of the barite inclusions (Figure 8). Lastly, oxidative pyrite weathering as additional sulfate source is inconsistent with a nearly oxygen-free Archean
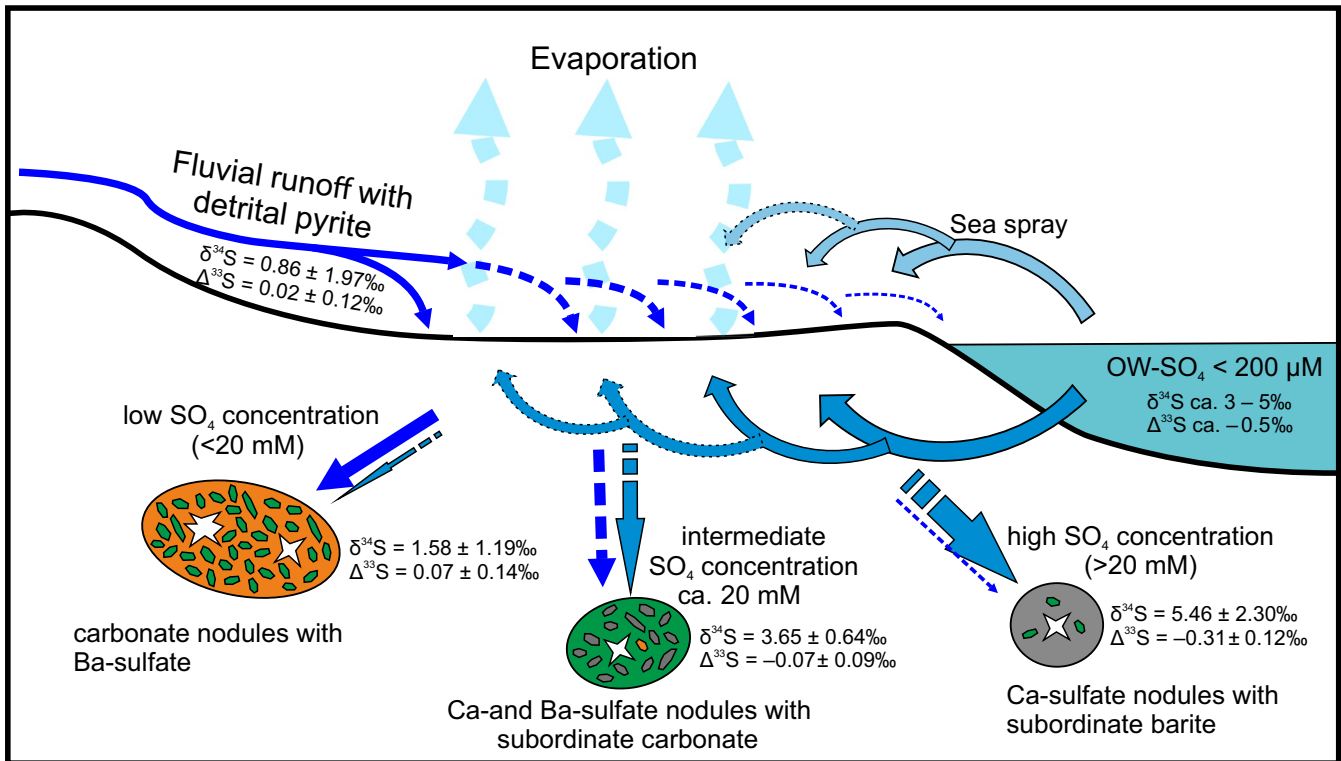
FIGURE 12 Schematic sketch showing origin of nodules with different mineralogy and S-isotopic composition in Moodies floodplain settings. Most sulfate accumulating in Moodies floodplains (ca. 3.22 Ga) was probably delivered by seawater that presumably had a similar S-isotopic signature as in Fig Tree times (ca. 3.26 Ga). The S-isotopic composition of anhydrite inclusions represents this contribution best; they likely formed by processes concentrating Archean seawater. Nodules composed of carbonate and barite, in contrast, formed at low sulfate concentrations and show a S-isotopic signature akin to that of detrital pyrite, indicating that oxidative pyrite weathering was an important, albeit minor, source of sulfate. Nodules composed of barite and anhydrite that formed at intermediate and possibly fluctuating sulfate concentrations show a S-isotopic signature indicative of mixing between seawater sulfate and sulfate produced by oxidative pyrite weathering

atmosphere as further backed up by the mainly negative $\Delta^{33}S$ values of the anhydrite. It is also unlikely because of the occurrence of detrital pyrite that is mostly well-rounded as typical for mechanical weathering (Figure S2). However, some pyrite grains show irregular shapes indicative of chemical alteration (Figure S2b). Additionally, the S-isotopic composition of the barite in sample 13-004-3 overlaps largely with that of the detrital pyrite from 12-003-4 (Figures 8a and 9), thus implying a connection between the two populations. In addition, detrital pyrite can repeatedly be found forming the majority of heavy mineral laminae in nodule-bearing beds (Figure S1). This indicates that oxidative pyrite weathering might have locally contributed a large proportion of sulfate to form the barite in sample 13-004-3 but only a minor fraction of sulfate delivered to the Moodies floodplains (Figure 12). Local production of free oxygen during so-called "whiffs" would not affect global MIF signals or the detrital mineral record if efficient consumption through reactions with sulfides or other reduced compounds prevented the O_2 flux to the atmosphere. Local and limited oxidative pyrite weathering might thus be possible despite the Archean geochemical record that argues for widespread anoxia in the atmosphere and oceans.

The barite inclusions from sample 13-004-4 show a homogeneous isotopic composition and an overlap of their $\delta^{34}S$ values with

the lightest values from sample 12-003-4 and the heaviest $\delta^{34}S$ values of sample 13-004-3 (Figure 8). Their $\Delta^{33}S$ values are less negative than those recorded in barite deposits from the underlying Fig Tree Group that are approximately 20 to 40 million years older (Figure 8b). Also, the lightest $\delta^{34}S$ values of this sample show a slight deviation from the mean composition, similar to that observed in sample 13-004-3, that might point toward the involvement of the same sulfate source for both samples. The presence of anhydrite and barite in this sample in approximately equal proportions suggests that the sulfate concentrations during its formation were between the two end-members represented by the other samples. Thus, the barite inclusions of sample 13-004-4 most likely represent a S-isotopic composition resulting from mixing of Archean seawater sulfate with sulfate potentially produced by oxidative pyrite weathering (Figure 12).

6.4 | Implications for the Archean sulfur cycle

The negative MIF signal of the Paleoarchean sulfates shows an apparent evolution over time with average $\Delta^{33}S$ values clustering around −1.3‰ at ca. 3.5 Ga and less negative $\Delta^{33}S$ values of

approximately −0.5‰ at ca. 3.26 Ga (Figure 8b; Bao et al., 2007; Farquhar et al., 2001; Hoering, 1989; Muller et al., 2017; Roerdink et al., 2012; Shen et al., 2009; Ueno et al., 2008). The $\Delta^{33}S$ isotopic signature of the anhydrite inclusions measured here (ca. −0.28‰), which likely represents seawater sulfate at the time of the Moodies deposition (ca. 3.22 Ga), is consistent with this trend and extends it to slightly younger ages. These observed differences in the Paleoarchean MIF signature are controversially debated and suggested to result from variations in volcanic activity (Philippot et al., 2012), changes in atmospheric composition (Claire et al., 2016; Halevy, Johnston, & Schrag, 2010; Whitehill et al., 2013), or a combination of both linked to differences in the depositional setting (Muller et al., 2016). Our data are unable to resolve processes responsible for this temporal trend, but appear to be consistent with input from a seawater sulfate source where they show similarity to the barite record. However, the Moodies nodules are in the most proximal position to a continental source of all Paleoarchean sulfates analyzed to date and occur in fluvially dominated environments with high depositional rates. As a result, Moodies sulfates should be more susceptible to short-term temporal and local spatial isotopic variability than the marine record. The Moodies Group may thus offer valuable locations for tracing the possible influence of atmospheric sulfur contribution and microbial processing on the Archean sulfur cycle.

6.5 | Implications for microbial activity

The $\delta^{34}S_{sulfate}$–$\delta^{34}S_{sulfide}$ fractionation of up to 34‰ between the pyrite overgrowths and corresponding anhydrite, and the constantly negative and strongly overlapping $\Delta^{33}S$ values of both minerals, shows a clear MDF effect recorded in the overgrowths (Figures 7 and 8). This isotope effect is consistent with biological processing, such as microbial sulfate reduction, as previously suggested based on their $\delta^{34}S$ composition (Nabhan, Wiedenbeck, et al., 2016). The occurrence of pyrite overgrowths only in the presence of $\delta^{34}S$-heavy anhydrite and barite (up to +10.45‰) agrees with an early-diagenetic formation. Such a large fractionation in this setting, if reflective of a single reduction step, is also consistent with sulfate concentrations < 5 μM as proposed for the Archean ocean (Bradley et al., 2016; Crowe et al., 2014; Eickmann et al., 2018; Wing & Halevy, 2014) but more easily achievable at the high sulfate concentrations that we infer for the Moodies floodplains.

The potential supply of additional sulfate by oxidative pyrite weathering that we suggest here appears to conflicts with the occurrence of well-rounded detrital pyrite grains in the same depositional system. The detrital pyrite lacks iron-oxide layers as previously recorded in the ca. 3.4 Ga-old basal sandstone of the Strelley Pool Fm., Pilbara Craton, Western Australia (Wacey, Saunders, Brasier, & Kilburn, 2011), that are indicative of oxidative weathering. However, some pyrite grains show irregular shapes indicative of chemical alteration (Figure S2b) and inclusions of carbonaceous matter close to their core–rim boundaries (Figure 7) that indicate a possible biogenic involvement. These inclusions of carbonaceous matter exclusively within the detrital part but mostly in contact to the overgrowths must have formed prior to the overgrowths. They could either be inherited from the source rock or result from microbial mediation of pyrite in Moodies sediment. A weak contribution of sulfate by microbial sulfur oxidation (MSO) using NO_3 as electron acceptor could be possible in this fluvially dominated environment. Based on geological evidence, MSO could be as old as ca. 3.5 Ga (Havig, Hamilton, Bachan, & Kump, 2017; Wacey et al., 2011) while estimates based on molecular clock calculations remain inconclusive (Havig et al., 2017). Sufficient availability of fixed nitrogen in nearby fluvial environments of the Moodies Group has been demonstrated based on bulk N-isotopic compositions between 2‰ and 5‰ of terrestrial microbial mats (Homann et al., 2018), and biological nitrogen fixation has been proposed to occur at least since the end of the Paleoarchean (ca. 3.2 Ga; Stüeken, Buick, Guy, & Koehler, 2015; Thomazo, Couradeau, & Garcia-Pichel, 2018). The shallow Archean ocean around 3.25 Ga to 2.95 Ga has also been shown to be locally mildly oxidizing based on the U content and Fe-isotopic composition of banded iron formations from the Fig Tree Group (Satkoski, Beukes, Li, Beard, & Johnson, 2015) and on the Fe- and S-isotopic composition of pyrite in stromatolites within tidal deposits of the Nsuze Group, Pongola Supergroup (Eickmann et al., 2018). Such mildly oxidizing seawater could also contribute to the oxidation of detrital pyrite. Solely abiotic oxidation would most likely be too slow to produce sufficient sulfate to explain the formation of barite with an almost identical S-isotopic signature as the detrital pyrite. Microbial sulfur oxidation can oxidize small proportions of pyrite and even introduce small portions of $\Delta^{33}S$-positive sulfate by oxidizing available S_0 aerosols. The metabolic effect on the $\Delta^{33}S$ values is minor (Zerkle, Farquhar, Johnston, Cox, & Canfield, 2009); the observed higher S-isotopic values of the barite would be a result of mixing $\Delta^{33}S$-negative seawater sulfate with the MSO-processed pyrite. $\delta^{34}S$ variations caused by MSO are less than 5‰ but result generally in slightly $\delta^{34}S$-depleted sulfate compared to the oxidized species (H_2S or S_0; Zerkle et al., 2009; Brabec, Lyons, & Mandernack, 2012). Therefore, MSO may have been the provider for the proposed additional sulfate source although its activity is mostly masked by the dominating evaporative-enriched seawater sulfate.

7 | CONCLUSIONS

The presence of anhydrite inclusions and quartz pseudomorphs after gypsum in ca. 3.22 Ga-old Moodies nodules shows that sulfate concentrations were locally highly elevated with respect to Archean seawater. The fluvial-to-supratidal depositional environment and S-isotopic composition of anhydrite, similar to marine barite of the Fig Tree Group, indicate that seawater was the likely sulfate source. Textural and mineralogical variations reflect changes in sulfate availability within the supratidal Moodies floodplains and are accompanied by variations in the S-isotopic composition of the sulfates. The

shift towards a juvenile isotopic signal of barite in former carbonate-dominated nodules that formed at low sulfate concentration shows the involvement of a secondary but minor sulfate source decoupled from seawater. The overlap and similarity in distribution of barite S-isotopic values to those of detrital pyrite indicate minor pyrite weathering under weakly oxidizing conditions. This oxidation might have been related to MSO using NO_3 as electron acceptor. The co-appearance of $\delta^{34}S$ heavy anhydrite and pyrite overgrowth with light $\delta^{34}S$ values and similar $\Delta^{33}S$ values strongly indicates the involvement of MSR in the formation of the early-diagenetic pyrite overgrowths.

ACKNOWLEDGMENTS

CONFLICT OF INTEREST

The authors declare no conflict of interest.

ORCID

Sami Nabhan (iD) https://orcid.org/0000-0001-7399-5131
Johanna Marin-Carbonne (iD) https://orcid.org/0000-0002-4265-1595
Paul R.D. Mason (iD) https://orcid.org/0000-0001-7569-5917

REFERENCES

Agangi, A., Hofmann, A., Eickmann, B., Marin-Carbonne, J., & Reddy, S. M. (2016). An atmospheric source of S in Mesoarchaean structurally-controlled gold mineralisation of the Barberton Greenstone Belt. *Precambrian Research 285*, 10–20.

Agangi, A., Hofmann, A., & Przybyłowicz, W. (2014). Trace element zoning of sulfides and quartz at Sheba and Fairview gold mines: Clues to Mesoarchean mineralisation in the Barberton Greenstone Belt, South Africa. *Ore Geology Reviews, 56*, 94–114.

Anhaeusser, C. R. (1976). The geology of the Sheba Hills area of the Barberton Mountain Land, South Africa, with particular reference to the Eureka Syncline. *Transactions of the Geological Society of South Africa, 79*, 253–280.

Aoya, M., Kouketsu, Y., Endo, S., Shimizu, H., Mizukami, T., Nakamura, D., & Wallis, S. (2010). Extending the application of Raman carbonaceous-material geothermometer using data from contact metamorphic rocks. *J. Metamorphic Geol., 28*, 895–914.

Babel, M., & Schreiber, B. C. (2014). Geochemistry of evaporites and evolution of seawater. In H. D. Holland, & K. K. Turekian (Eds.), *Treatise on geochemistry*, Vol. *9*, 2nd ed. (pp. 483–560). Amsterdam, the Netherlands: Elsevier.

Bao, H., Rumble, D. III, & Lowe, D. R. (2007). The five stable isotope compositions of Fig Tree barites: Implications on sulfur cycle in ca. 3.2 Ga oceans. *Geochimica Et Cosmochimica Acta, 71*, 4868–4879.

Beyssac, O., Goffe, B., Chopin, C., & Rouzaud, J. N. (2002). Raman spectra of carbonaceous material from metasediments: A new geothermometer. *J. Metamorphic Geol., 20*, 859–871.

Bock, E. (1961). On the solubility of anhydrous calcium sulphate and of gypsum in concentrated solutions of sodium chloride at 25 °C, 30 °C, 40 °C, and 50 °C. *Canadian Journal of Chemistry, 39*, 1746–1751.

Brabec, M. Y., Lyons, T. W., & Mandernack, K. W. (2012). Oxygen and sulfur isotope fractionation during sulfide oxidation by anoxygenic phototrophic bacteria. *Geochimica Et Cosmochimica Acta, 83*, 234–251.

Bradley, A. S., Leavitt, W. D., Schmidt, M., Knoll, A. H., Girguis, P. R., & Johnston, D. T. (2016). Patterns of sulfur isotope fractionation during microbial sulfate reduction. *Geobiology, 14*, 91–101.

Buick, R., & Dunlop, J. S. R. (1990). Evaporite sediments of early Archaean age from the Warrawoona Group, North Pole, Western Australia. *Sedimentology, 37*, 247–277.

Byerly, G. R., Lowe, D. R., & Heubeck, C.(2018) Geologic evolution of the Barberton Greenstone Belt – a unique record of crustal development, surface processes, and early life 3.55 to 3.20 Ga. In: M. J. Van Kranendonk, V. C. Bennett & J. E. Hoffmann (Eds.), *Earth's Oldest Rocks – Second Edition* (pp. 569–613). Amsterdam: Elsevier.

Cameron, E. M. (1983). Evidence from early Proterozoic anhydrite for sulphur isotopic partitioning in Precambrian oceans. *Nature, 304*, 54–56.

Cameron, E. M., & Hattori, K. (1987). Archean Sulphur cycle: Evidence from sulphate minerals and isotopically fractionated sulphides in Superior Province, Canada. *Chemical Geology: Isotope Geoscience Section, 65*, 341–358.

Canfield, D. E., Habicht, K. S., & Thamdrup, B. (2000). The Archean sulfur cycle and the early history of atmospheric oxygen. *Science, 288*, 658–661.

Chandler, F. W. (1988). Diagenesis of sabkha-related, sulphate nodules in the Early Proterozoic Gordon Lake Formation. *Ontario, Canada, Carbonates and Evaporites, 3*, 75–94.

Chowns, T. M., & Elkins, J. E. (1974). The origin of quartz geodes and cauliflower chert through silicification of anhydrite nodules. *Journal of Sedimentology Petrology, 44*, 885–903.

Claire, M. W., Kasting, J. F., Domagal-Goldman, S. D., Stüeken, E. E., Buick, R., & Meadows, V. S. (2016). Modeling the signature of sulfur mass-independent fractionation produced in the Archean atmosphere. *Geochimica Et Cosmochimica Acta, 141*, 365–380.

Crowe, S. A., Paris, G., Katsev, S., Jones, C. A., Kim, S.-T., Zerkle, A. L., … Canfield, D. E. (2014). Sulfate was a trace constituent of Archean seawater. *Science, 346*, 735–739.

da Burron, I., Costa, G., Sharpe, R., Fayek, M., Gauert, C., & Hofmann, A. (2018). 3.2 Ga detrital uraninite in the Witwatersrand Basin, south Africa: Evidence of reducing Archean atmosphere. *Geology, 46*, 295–298.

Davis, J. W., & Collins, A. G. (1971). Solubility of barium and strontium sulfates in strong electrolyte solutions. *Environmental Science & Technology, 5*, 1039–1043.

de Ronde, C. E. J., Spooner, E. T. C., de Wit, M. J., & Bray, C. J. (1992). Shear zone-related, Au quartz vein deposits in the Barberton greenstone belt, South Africa; field and petrographic characteristics, fluid properties, and light stable isotope geochemistry. *Economic Geology, 87*, 366–402.

Eickmann, B., Hofmann, A., Wille, M., Bui, T. H., Boswell, A. W., & Schoenberg, R. (2018). Isotopic evidence for oxygenated Mesoarchean shallow oceans. *Nature Geoscience, 11*, 133–138.

England, G. L., Rasmussen, B., Krapez, B., & Groves, D. I. (2002). Palaeoenvironmental significance of rounded pyrite in siliciclastic sequences of the Late Archaean Witwatersrand Basin: Oxygen-deficient atmosphere or hydrothermal alteration? *Sedimentology*, *49*, 1133–1156.

Farquhar, J., Bao, H., & Thiemens, M. H. (2000). Atmospheric influence of Earth's earliest sulfur cycle. *Science*, *289*, 756–758.

Farquhar, J., Peters, M., Johnston, D. T., Strauss, H., Masterson, A., Wichert, U., & Kaufman, A. J. (2007). Isotopic evidence for Mesoarchean anoxia and changing atmospheric Sulphur chemistry. *Nature*, *449*, 706–710.

Farquhar, J., Savarino, J., Airieau, S., & Thiemens, M. H. (2001). Observation of wavelength sensitive mass-independent sulfur isotope effects during SO2 photolysis: Implications for the early atmosphere. *Journal of Geophysical Research*, *106*, 32829–32839.

Farquhar, J., & Wing, B. A. (2003). Multiple sulfur isotopes and the evolution of the atmosphere. *Earth and Planetary Science Letters*, *213*, 1–13.

Golding, L. Y., & Walter, M. R. (1979). Evidence of evaporite minerals in the Archaean Black Flag beds, Kalgoorlie, Western Australia, BMR. *Journal of Geology and Geophysics*, *4*, 67–71.

Gregory, D., Large, R., Halpin, J., Steadman, J., Hickman, A., Ireland, T., & Holden, P. (2015). The chemical conditions of the late Archean Hamersley basin inferred from whole rock and pyrite geochemistry with Δ^{33}S and δ^{34}S isotope analyses. *Geochimica Et Cosmochimica Acta*, *149*, 223–250.

Grosch, E. G., & McLaughlin, N. (2013). Paleoarchean sulfur cycle and biogeochemical surface conditions on the early Earth, Barberton, South Africa. *Earth and Planetary Science Letters*, *377–378*, 142–154.

Guy, B. M., Ono, S., Gutzmer, J., Kaufman, A. J., Lin, Y., Fogel, M. L., & Beukes, N. J. (2012). A multiple sulfur and organic carbon isotope record from non-conglomeratic sedimentary rocks of the Mesoarchean Witwatersrand Supergroup, South Africa. *Precambrian Research*, *216–219*, 208–231.

Habicht, K. S., Gade, M., Thamdrup, B., Berg, P., & Canfield, D. E. (2002). Calibration of sulfate levels in the Archean Ocean. *Science*, *298*, 2372–2374.

Halevy, I., Johnston, D. T., & Schrag, D. P. (2010). Explaining the structure of the Archean mass-independent sulfur isotope record. *Science*, *329*, 204–207.

Havig, J. R., Hamilton, T. L., Bachan, A., & Kump, L. R. (2017). Sulfur and carbon isotopic evidence for metabolic pathway evolution and a four-stepped Earth system progression across the Archean and Paleoproterozoic. *Earth-Science Reviews*, *174*, 1–21.

Heinrichs, T. K., & Reimer, T. (1977). A sedimentary barite deposit from the Archean Fig Tree Group of the Barberton Mountain Land (South Africa). *Economic Geology*, *72*, 1426–1441.

Heubeck, C. (2019). The Moodies Group—a High-Resolution Archive of Archaean Surface Processes and Basin-Forming Mechanisms. In: Kröner, A., Hofmann, A., (Eds.), The Archaean Geology of the Kaapvaal Craton, Southern Africa. Springer (Regional Geology Reviews). Cham, Switzerland, pp. 133–169.

Heubeck, C., Bläsing, S., Grund, M., Drabon, N., Homann, M., & Nabhan, S. (2016). Geological constraints on Archean (3.22 Ga) coastal-zone processes from the Dycedale Syncline, Barberton Greenstone Belt. *South African Journal of Geology*, *119*, 495–518.

Heubeck, C., & Lowe, D. R. (1999). Sedimentary petrology and provenance of the Archean Moodies Group, Barberton Greenstone Belt, South Africa. In D. R. Lowe, & G. R. Byerly (Eds.), *Geologic Evolution of the Barberton Greenstone Belt, South Africa*, *329* (pp. 259–286). Boulder, Colorado: Geological Society of America Special Paper.

Hoering, T. C. (1989). The isotopic composition of bedded barites from the Archean of Southern India. *Journal of the Geological Society of India*, *34*, 461–466.

Hofmann, A., Bekker, A., Rouxel, O., Rumble, D., & Master, S. (2009). Multiple sulfur and iron isotope composition of detrital pyrite in Archaean sedimentary rocks: A new tool for provenance analysis. *Earth and Planetary Science Letters*, *286*, 436–445.

Homann, M., Sansjofre, P., Van Zuilen, M., Heubeck, C., Gong, J., Killingsworth, B., ... Lalonde, S. V. (2018). Microbial life and biogeochemical cycling on land 3,220 million years ago. *Nature Geoscience*, *11*, 665–671.

Huston, D. L., & Logan, G. A. (2004). Barite, BIFs and bugs: Evidence for the evolution of the Earth's early hydrosphere. *Earth and Planetary Science Letters*, *220*, 41–55.

Kasting, J. F. (2001). The rise of atmospheric oxygen. *Science*, *293*, 819–820.

Knauth, L. P. (2005). Temperature and salinity history of the Precambrian ocean: Implications for the course of microbial evolution. *Palaeogeography, Palaeoclimatology, Palaeoecology*, *219*, 53–69.

Koglin, N., Frimmel, H. E., Minter, W. E. L., & Brätz, H. (2010). Trace-element characteristics of different pyrite types in Mesoarchaean to Palaeoproterozoic placer deposits. *Mineralium Deposita*, *45*, 259–280.

Large, R. R., Danyushevsky, L., Hollit, C., Maslennikov, V., Meffre, S., Gilbert, S., ... Foster, J. (2009). Gold and trace element zonation in pyrite using a laser imaging technique: Implications for the timing of gold in orogenic and Carlin-style sediment-hosted deposits. *Economic Geology*, *104*, 635–668.

Lowe, D. R., & Byerly, G. R. (2007). An overview of the geology of the Barberton Greenstone Belt and vicinity: Implications for early crustal development. In M. J. van Kranendonk, R. H. Smithies, & V. H. Bennett (Eds.), *Earth's Oldest Rocks*, *15* (pp. 481–526). Amsterdam: Elsevier (Developments in Precambrian Geology).

Lowe, D. R., Byerly, G. R., & Heubeck, C. (1999). Structural divisions and development of the west-central part of the Barberton Greenstone Belt. In D. R. Lowe, & G. R. Byerly (Eds.), *Geologic Evolution of the Barberton Greenstone Belt, South Africa*, *329* (pp. 37–82). Boulder, Colorado: Geological Society of America Special Paper.

Lowe, D. R., Drabon, N., & Byerly, G. R. (2019). Crustal fracturing, unconformities, and barite deposition, 3.26–3.23 Ga, Barberton Greenstone Belt. *South Africa. Precambrian Res.*, *327*, 34–46.

Lowe, D. R., & Worrell, G. F. (1999). Sedimentology, mineralogy and implications of silicified evaporites in the Kromberg Formation, Barberton Greenstone Belt, South Africa. *Geological Society of America Special Paper*, *329*, 167–188.

Machel, H. G. (2001). Bacterial and thermochemical sulfate reduction in diagenetic settings – old and new insights. *Sedimentary Geology*, *140*, 143–175.

Mack, G. H., James, W. C., & Monger, H. C. (1993). Classification of paleosols. GSA. *Bulletin*, *105*, 129–136.

Marin-Carbonne, J., Rollion-Bard, C., Bekker, A., Rouxel, O., Agangi, A., Cavalazzi, B., ... McKeegan, K. D. (2014). Coupled Fe and S isotope variations in pyrite nodules from Archean shale. *Earth and Planetary Science Letters*, *392*, 67–79.

Marty, B., Avice, G., Bekaert, D. V., & Broadley, M. W. (2018). Salinity of the Archean ocean from analysis of fluid inclusions in quartz. *C. R. Geoscience*, *350*, 154–163.

Mojzsis, S. J., Coath, C. D., Greenwood, J. P., McKeegan, K. D., & Harrison, T. M. (2003). Mass-independent isotope effects in Archean (2.5 to 3.8 Ga) sedimentary sulfides determined by ion microprobe analysis. *Geochimica Et Cosmochimica Acta*, *67*, 1635–1658.

Muller, É., Philippot, P., Rollion-Bard, C., & Cartigny, P. (2016). Multiple sulfur-isotope signatures in Archean sulfates and their implications for the chemistry and dynamics of the early atmosphere. *Proc. Nat. Acad. Sci.*, *113*, 7432–7437.

Muller, E., Philippot, P., Rollion-Bard, C., Cartigny, P., Assayag, N., Marin-Carbonne, J., ... Sarma, D. S. (2017). Primary sulfur isotope signatures preserved in high-grade Archean barite deposits of the Sargur Group, Dharwar Craton. *India. Precambrian Res.*, *295*, 38–47.

Nabhan, S., Luber, T., Scheffler, F., & Heubeck, C. (2016a). Climatic and geochemical implications of Archean pedogenic gypsum of the

Moodies Group (~3.2 Ga), Barberton Greenstone Belt. *South Africa. Precambrian Res.*, *275*, 119–134.

Nabhan, S., Wiedenbeck, M., Milke, R., & Heubeck, C. (2016b). Biogenic overgrowth on detrital pyrite in 3.2 Ga Archean paleosols. *Geology*, *44*, 763–766.

Ohmoto, H., Kakegawa, T., & Lowe, D. R. (1993). 3.4-billion-year old biogenic pyrites from Barberton. *South Africa: Sulfur Isotope Evidence. Science*, *262*, 555–557.

Otto, A., Dziggel, A., Kisters, A., & Meyer, F. (2007). The New Consort Gold Mine, Barberton greenstone belt, South Africa: Orogenic gold mineralization in a condensed metamorphic profile. *Mineralium Deposita*, *42*, 715–735.

Partridge, E. P., & White, A. H. (1929). The solubility of calcium sulfate from 0 to 200 degrees. *Journal of the American Chemical Society*, *51*, 360–370.

Pavlov, A. A., & Kasting, J. F. (2002). Mass-independent fractionation of sulfur isotopes in Archean sediments: Strong evidence for an anoxic Archean atmosphere. *Astrobiology*, *2*, 27–41.

Philippot, P., Van Zuilen, M., Lepot, K., Thomazo, C., Farquhar, J., & Van Kranendonk, M. J. (2007). Early Archaean microorganisms preferred elemental sulfur, not sulfate. *Science*, *317*, 1534–1537.

Philippot, P., van Zuilen, M., & Rollion-Bard, C. (2012). Variations in atmospheric Sulphur chemistry on early Earth linked to volcanic activity. *Nature Geoscience*, *5*, 668–674.

Reimer, T. O. (1980). Archean sedimentary baryte deposits of the Swaziland Supergroup (Barberton Mountain Land, South Africa). *Precambrian Res.*, *12*, 393–410.

Reimer, T. O. (1990). Archaean baryte deposits of Southern Africa. *Journal of the Geological Society of India*, *35*, 131–150.

Retallack, G. J. (1991). Untangling the effects of burial alteration and ancient soil formation. *Annual Review of Earth and Planetary Sciences*, *19*, 183–206.

Retallack, G. J. (1993). Classification of paleosols: Discussion and reply. *GSA Bulletin*, *105*, 1635–1637.

Roerdink, D. L., Mason, P. R. D., Farquhar, J., & Reimer, T. (2012). Multiple sulfur isotopes in paleoarchean barites identify an important role for microbial sulfate reduction in the early marine environment. *Earth and Planetary Science Letters*, *331*, 177–186.

Roerdink, D. L., Mason, P. R. D., Whitehouse, M. J., & Brouwer, F. M. (2016). Reworking of atmospheric sulfur in a Paleoarchean hydrothermal system at Londozi, Barberton Greenstone Belt. *Swaziland. Precambrian Res.*, *280*, 195–204.

Roerdink, D. L., Mason, P. R. D., Whitehouse, M. J., & Reimer, T. (2013). High-resolution quadruple sulfur isotope analyses of 3.2Ga pyrite from the Barberton Greenstone Belt in South Africa reveal distinct environmental controls on sulfide isotopic arrays. *Geochimica Et Cosmochimica Acta*, *117*, 203–215.

Rye, R. O. (2005). A review of the stable-isotope geochemistry of sulfate minerals in selected igneous environments and related hydrothermal systems. *Chemical Geology*, *215*, 5–36.

Satkoski, A. M., Beukes, N. J., Li, W., Beard, B. L., & Johnson, C. M. (2015). A redox-stratified ocean 3.2 billion years ago. *Earth and Planetary Sciece Letters*, *430*, 43–53.

Shen, Y. N., Farquhar, J., Masterson, A., Kaufman, A. J., & Buick, R. (2009). Evaluating the role of microbial sulfate reduction in the early Archean using quadruple isotope systematics. *Earth and Planetary Science Letters*, *279*, 383–391.

Sighinolfi, G. P., Kronberg, B. I., Gorgoni, C., & Fyfe, W. S. (1980). Geochemistry and genesis of sulphide-anhydrite-bearing Archean carbonate rocks from Bahia (Brazil). *Chemical Geology*, *29*, 323–331.

Strauss, H., Melezhik, V. A., Reuschel, M., Fallick, A. E., Lepland, A., Rychanchik, D. V. et al (2013). Abundant Marine Calcium Sulphates: Radical Change of Seawater Sulphate Reservoir and Sulphur Cycle. In V. Melezhik (Ed.), *Reading the Archive of Earth's Oxygenation*. Springer, Berlin, Heidelberg: Frontiers in Earth Sciences.

Stüeken, E., Buick, R., Guy, B. M., & Koehler, M. C. (2015). Isotopic evidence for biological nitrogen fixation by molybdenum-nitrogenase from 3.2 Gyr. *Nature*, *520*, 666–669.

Thomassot, E., Cartigny, P., Harris, J. W., Lorand, J. P., Rollion-Bard, C., & Chaussidon, M. (2009). Metasomatic diamond growth: A multi-isotope study (^{13}C, ^{15}N, ^{33}S, ^{34}S) of sulphide inclusions and their host diamonds from Jwaneng (Botswana). *Earth and Planetary Science Letters*, *282*, 79–90.

Thomazo, C., Couradeau, E., & Garcia-Pichel, F. (2018). Possible nitrogen fertilization of the early Earth Ocean by microbial continental ecosystems. *Nature Communications*, *9*, 2530.

Ueno, Y., Ono, S., Rumble, D., & Maruyama, S. (2008). Quadruple sulfur isotope analysis of ca. 3.5 Ga Dresser Formation: New evidence for microbial sulfate reduction in the early Archean. *Geochimica Et Cosmochimica Acta*, *72*, 5675–5691.

Wacey, D., Saunders, M., Brasier, M. D., & Kilburn, M. R. (2011). Earliest microbially mediated pyrite oxidation in ~3.4 billion-year-old sediments. *Earth and Planetary Science Letters*, *301*, 393–402.

Whitehill, A. R., Xie, C., Hu, X., Xie, D., Guo, H., & Ono, S. (2013). Vibronic origin of sulfur mass-independent isotope effect in photoexcitation of SO_2 and the implications to the early earth's atmosphere. *Proceedings of the National Academy of Sciences*, *110*, 17697–17702.

Wing, B. A., & Halevy, I. (2014). Intracellular metabolite levels shape sulfur isotope fractionation during microbial sulfate respiration. *PNAS*, *111*, 18116–18125.

Worden, R. H., Smalley, P. C., & Oxtoby, N. H. (1995). Gas souring by thermochemical sulfate reduction at 140°C Am. *Assoc. Pet. Geol. Bull.*, *79*, 854–863.

Zerkle, A. L., Farquhar, J., Johnston, D. T., Cox, R. P., & Canfield, D. E. (2009). Fractionation of multiple sulfur isotopes during phototrophic oxidation of sulfide and elemental sulfur by a green sulfur bacterium. *Geochimica Et Cosmochimica Acta*, *73*, 291–306.

SUPPORTING INFORMATION

Additional supporting information may be found online in the Supporting Information section.